UNIVERSITY OF TURKU

Electromagnetic Scattering Characteristics of Composite Targets and Software Development Based on PO Algorithm

Information and Communication Technology
Department of Computing, Faculty of Technology
Master of Science in Technology Thesis

Author(s):
Chuanmo Wang

Supervisor(s):
MSc (Tech) Qingqing Li
Assoc. Prof. Tomi Westerlund

June 2022
Turku

Master's thesis

Subject: Electromagnetic Computing
Author(s): Chuanmo Wang
Title: Electromagnetic Scattering Characteristics of Composite Targets and Software Development Based on PO Algorithm
Supervisor(s): MSc (Tech) Qingqing Li, Assoc. Prof. Tomi Westerlund
Number of pages: 64 pages
Date: June 2022

Abstract.

Physical optics (PO) algorithm is a high-frequency electromagnetic (EM) algorithm, which is widely used to solve the EM scattering problems of electrically large composite targets. Due to the PO algorithm only considers the induced current in the bright region irradiated by EM wave, the computational memory and time consumption are superior than other high-frequency algorithms, and the calculation accuracy is pretty fine. Based on the PO algorithm, this thesis focuses on the occlusion judgement of PO algorithm and its application in composite targets. The main contents of this thesis are as follows:

1. The occlusion judgement software system for PO algorithm is developed. The main function of this software is to judge the bright region of the target under the irradiation of EM wave. This software uses two judgement methods: ray tracing method based on CPU and Z-Buffer method based on CPU and GPU. Moreover, due to the compromise between patch size and patch number, both methods have errors at the edge of bright and shadow regions. This thesis discusses the error and reduces it.

2. Based on PO algorithm, the EM scattering characteristics of targets covered by plasma sheath are discussed. We simulate the plasma sheath flow field data of hypersonic vehicle by FASTRAN software, compare and analyze the plasma sheath electron number density at different flight heights and speeds. On this basis, the bistatic RCS of hypersonic vehicle head-on irradiation under different flight heights and speeds is calculated by using the PO algorithm of layered medium.

3. SAR image simulation of tree ground composite target is carried out based on PO algorithm and Non-Uniform Fast Fourier Transform (NUFFT) method. Firstly, we introduce the geometric modeling and EM parameter modeling of tree ground composite target, and the scattering characteristics of tree ground composite target are obtained by using PO algorithm. Finally, the scattering field of the target is processed by NUFFT method, and the SAR simulation images of multiple trees scene are obtained.

Key words: PO algorithm, EM Scattering, Z-Buffer frame cache, Plasma sheath, SAR image simulation.

Table of contents

1 Introduction

1.1 Research Background and Significance

In the fields of national defense and civilian (such as remote sensing imaging, geological disaster prevention and forest protection), the analysis of electromagnetic (EM) scattering characteristics of composite targets composed of dielectric and perfect electric conductor (PEC) has become more and more closely related to people's daily life. Moreover, the study of EM scattering characteristics will also drive the development of basic disciplines and research. Therefore, the analysis on EM scattering characteristics of composite targets plays an important role and has great academic value.

In practical EM scattering problems, due to the various material and the irregular shape of different targets, it is difficult to use the classical Maxwell equation method directly in calculation [1]. However, with the vigorous development of computer technology, computational electromagnetism has produced a variety of algorithms with the support of the powerful computing function of the computer, such as the method of moments (MOM) of the integral equation method, the finite difference time domain (FDTD) of the differential equation method, or the physical optics (PO) and geometric optics (GO) of the high frequency approximation method. PO algorithm is one of the typical high-frequency methods. The basic principle of PO algorithm is to express the scattering field of EM target in the integral form of induced surface current on the target surface, and determine the induced surface current on the target surface by geometric approximation. Due to the PO algorithm ignores the surface current in the shadow region, the accuracy of the occlusion judgement plays important role when using the PO algorithm to solve the scattering characteristics of electrically large targets [2].

PO algorithm can solve the scattering field of composite target, and the interaction mechanism between radar wave and composite target can be obtained through scattering field analysis. When radar is used to scan the composite target such as plasma sheath covering vehicle or forest ground complex target, a large amount of information related to the scatterer itself is included in the radar echo [3], including the flow field conditions around the vehicle, the vehicle shape, density of trees in forest, water content and dielectric constant of surface soil, etc. At present, the difficulty in composite target scattering research is that when radar detects composite targets, the scattering echo will not only contain the scattering information of the target's own attributes, but also mix with other information such as dielectric layer parameters, which will cause great interference to the accurate analysis of the target's space position, shape or motion state, so that

it is hard to detect or image the target effectively. Therefore, the study on the interaction mechanism between radar wave and composite target can provide necessary theoretical support and effective research methods for hypersonic target communication and SAR image simulation.

1.1.1 Plasma Sheath Covering Hypersonic Vehicle

When a hypersonic vehicle flies in the air, the temperature is highly enough to make the air dissociation and ionization. And this will create a very complex ionosphere on the surface of the aircraft, with a peak electron number density of $10^{13}cm^{-3}$~$10^{15}cm^{-3}$ and a dozen chemical components, known as plasma sheath [4]. As early as the 1960s, the United States carried out a series of reentry flight experiments such as RAM [5][6]. In the experiments, the plasma electron density and Ka band reflection coefficient were measured, and a large number of experimental data were obtained. In the experiment, owing to the existence of plasma sheath, the power of the EM wave was attenuated and its original physical properties was changed, so the EM wave may be refracted, reflected and scattered on the surface of the vehicle. Even during a certain period of reentering, radio communication between the vehicle and the ground will be completely lost, which is the "blackout" phenomenon [7]. Therefore, studying the EM scattering characteristics of plasma sheath covering vehicle will facilitate the radar detection and recognition of hypersonic target, communication and control with target.

1.1.2 SAR Image Simulation for Tree Ground Composite Target

For tree ground composite targets, with the development of remote sensing and Synthetic Aperture Radar (SAR) image simulation technology, the theoretical and applied research on EM scattering of tree composite scenes has attracted attention of many scholars. As an important way to obtain SAR image, SAR image simulation technology makes use of the powerful data processing ability of computer, low cost and easy to implement. It is crucial in the determination of imaging algorithm for SAR system parameters, performance and verification [8][9]. Feature based SAR image simulation focuses on the simulation of the geometric and radiation features of the image, and pursues the similarity between the simulated image and the real image, such as the shape and distribution of scattering points [10]. In order to get useful information from the scattering field and obtain the SAR simulation image accurately, it is necessary to fully consider the interaction mechanism between EM wave and various ground objects in the modeling process, and establish an effective model according to

the characteristics of different scatterer to eliminate interference on target scatterers, so as to achieve the purpose of accurate SAR image simulation.

1.2 Domestic and Abroad Research Status

1.2.1 Status on EM Simulation Software Development

EM simulation software can provide better calculation accuracy and efficiency, and its perfect human-computer interaction is also very helpful to software users. At present, western countries have successively developed their own high-frequency EM simulation software system. Xpatch [11] simulation software developed by US Defense EM Analysis company is the most mature military EM analysis software. Xpatch can simulate the EM target based on the Shooting and Bouncing Ray method (SBR). GRECO software developed by the Spanish space agency is to accelerate the calculation speed of EM targets with the help of Z-Buffer technology of imaging [12] The FASCRO software also use the Z-Buffer technology to accelerate the EM algorithm [13], which is based on the software acceleration idea of Z-Buffer in the ray tracing process.
In recent years, domestic high-frequency EM simulation software has also developed rapidly, including GRECO-CMT developed by Beijing University of Aeronautics and Astronautics, NESC developed by the State Key Laboratory of Millimeter Waves of Southeast University, EM simulation software on NURBS surface developed by Xi'an University of Electronic Science and technology, and EMCS of the second Academy of Astronautics. These software play an important role in the China’s national defense industry [14].

1.2.2 Status on EM Characteristics of Plasma Sheath

Since the 1960s, NASA has done detailed data acquisition and analysis on the whole ballistic process of RAM-C [15][16]. In the following decades, there has been little progress in EM characteristics of plasma sheath. Researchers began to pay more attention to this aspect of work in recent 15 years. In 2008, K. Schuler et al. used ray tracing method to study the EM scattering characteristics of vehicle targets [17]. In 2010, V. I. Sotnikov et al. analyzed the EM scattering characteristics caused by turbulence around the vehicle [18]. In 2014, M. Walter et al. studied the Doppler phenomenon caused by EM waves incident on flying targets [19]. In 2017, the EM wave scattering from an elliptical plasma cylinder in the presence of an external oblique magnetic field is investigated by S. Safari [20]. In 2020, D. R. Smith use the finite-difference time-domain (FDTD) method to solve the EM wave interactions with plasma irregularities within a polar cap patch [21].

The research on the EM scattering characteristics of plasma sheath in China started late. In 2008, Y. Chang et al. calculated the radar target scattering characteristics of the blunt head cone by using the Piecewise Linear Current Density Recursive Convolution - Finite Different Time Domain (PLJERC-FDTD) method [22]. In 2014, L. Nie and W. F. Chen of Zhejiang University numerically simulated the hypersonic plasma flow field using the seven component chemical reaction equations, and calculated the P-band and L-band backscattering cross sections using PLJERC-FDTD method [23]. At the same time, C. Zhou and X. K. Zhang of Air Force Engineering University studied the attenuation mechanism of plasma on EM wave by using FEKO and PO method, and analyzed the influence of reentry warhead coated plasma on RCS [24]. In 2020, Z. Bian et al. proposed the Inhomogeneity Zonal Medium Model (IZMM) to calculate and analyze the EM scattering characteristics of hypersonic vehicle covered with a plasma sheath [25].

1.2.3 Status on SAR Image Simulation

In the actual EM scattering calculation process, for complex targets or composite targets, a single EM calculation method usually couldn't accurately calculate the scattering field of the whole target. In 2010, K. F. Ji used PO method, PTD method and GO/PO hybrid method to simulate the SAR image of ground vehicle targets when calculating specular reflection, edge diffraction and multiple scattering [26]. In 2011, X. F. Zhang et al. used the PO method and the Incremental Length Diffraction Coefficient (ILDC) method to calculate the RCS of the edge in the panel [27]. Under the HH polarization mode, the scattered field is coherently superimposed and projected onto the SAR imaging plane to obtain the ship SAR image. In 2015, X. J. Wei shows the simulation results of incoherent simulation method for typical targets in [28]. GO method is used to track high-frequency EM rays, PO method is used to calculate EM scattering coefficient, and equivalent EM flow method is used to calculate edge scattering. Finally, the simulated SAR image is superimposed and projected, and the similarity with the real image is more than 70%. In papers [29][30][31], the authors use ray tracing technology to simulate SAR images of typical planar buildings, and considers the multipath scattering effect of building targets. In papers [32][33], they have improved the ray tracing method to accelerate the speed of ray tracing and realize the rapid simulation of SAR images.

1.3 Main Content and Chapter Arrangement

In this thesis, we mainly focus on the occlusion judgement of PO algorithm and the two applications of PO algorithm in plasma sheath covering hypersonic vehicle and tree ground composite target.The main research work of this thesis is divided into five chapters.

The first chapter is the introduction. This chapter mainly introduces the research background and significance of the scattering characteristics of the composite target, and explains the main work of this thesis, that is, developed the occlusion judgement software, discussed the EM scattering characteristics of the plasma sheath coated target and the EM scattering characteristics of the tree ground composite target. All of them are based on the PO algorithm. Then this chapter introduces the research status of EM simulation software, plasma sheath EM scattering characteristics and SAR imaging simulation both domestic and abroad. Finally, this chapter presents the main content detailed chapter arrangement of this thesis.

The second chapter is the development of occlusion judgement software. Firstly, we introduce the PO algorithm and verify it correctness for PO algorithm is the fundamental of this whole thesis. Secondly, we introduce two bright region search methods, namely, ray tracing method based on CPU and the Z-Buffer method based on CPU and GPU. Lastly, we optimize the bright region result by using the iterative method to segment the edge patches of bright and dark regions.

The third chapter is the study of EM scattering characteristics of plasma sheath coated hypersonic vehicle. This chapter mainly introduces the related concepts plasma sheath, PO algorithm for coating target and step method for reflection coefficient. Then, the flow field of blunt cone is simulated by FASTRAN software, and the electron number density, plasma frequency and collision frequency of plasma sheath are obtained. Finally, the bistatic RCS of plasma sheath coated targets in different flight altitudes and speeds are calculated, and the results are compared and analyzed.

The fourth chapter is the research on the EM scattering characteristics of tree ground composite targets. Firstly, we introduce the principle of SAR imaging briefly, then we get the dielectric characteristics of typical surface media such as vegetation and soil, next we obtain the EM scattering characteristic data according to the PO algorithm. Finally, we obtain the SAR image of tree ground composite scene.

The last chapter is the summary and prospect, summarizes the main contents and corresponding research results, and points out the existing problems and the research direction of the next step.

2 Software System for Occlusion Judgement in PO Algorithm

As mentioned in Chapter 1, the PO algorithm assumes that the induced current only exists in the region illuminated by the incident wave, so how to accurately judge the bright region of the scatterer is very important in this whole work [34]. Moreover, for such a complex software program with many inputs and outputs, writing a UI interface software system can greatly facilitate the user's operation. In this chapter, we use Qt5 to develop a UI interface for bright region search, which includes two methods, one is ray tracing method based on CPU, another one is the Z-Buffer depth cache technology based on CPU and GPU. Further, we segment the edge patch of the judgement result and continue to judge the bright region to make the result of the bright region more accurate. In this chapter, we first introduce the basic concept of RCS and the process of obtaining PEC target RCS by PO algorithm in detail. After the verification of PO algorithm, we introduce Qt5 and OpenGL API. Then we introduce two bright region search methods, and finally show the results of our occlusion judgement.

2.1 Basics of PO Algorithm

2.1.1 Basics of Radar Cross Section

When a target is incident by EM wave, the total EM field is consisted of the incident wave and scattered wave [35]. The spatial distribution of scattered energy depends on the shape, size and structure of the object, as well as the direction, polarization and frequency. This distribution of energy is called scattering, which is characterized by Radar Cross Section, an imaginary area of an object.

RCS is a measure of return or scattering power in a given direction, which is normalized by the power density of incident field. Formally, the Radar Cross Section is defined as

$$\sigma = \lim_{R\to\infty} 4\pi R^2 \frac{S_s}{S_i} = \lim_{R\to\infty} 4\pi R^2 \frac{\left|\boldsymbol{E}_s\right|^2}{\left|\boldsymbol{E}_i\right|^2} = \lim_{R\to\infty} 4\pi R^2 \frac{\left|\boldsymbol{H}_s\right|^2}{\left|\boldsymbol{H}_i\right|^2} \tag{2.1}$$

Where, S_s and S_i are the energy flux density of scattered wave at radar receiver and incident wave at the scatterer, respectively. $\boldsymbol{E}_s$ and $\boldsymbol{E}_i$ are the scattered electric field at radar receiver and incident electric field at the scatterer, respectively. $\boldsymbol{H}_s$ and $\boldsymbol{H}_i$ are the scattered magnetic field at radar receiver and incident magnetic field at the scatterer, respectively.

RCS is scalar, we can judge the correctness of the equation according to whether the dimension is the square of length. The common unit of RCS is "m^2", which is usually given in logarithmic

form, that is, the decibel relative to $1m^2$, recorded as dBsm. The conversion relationship between the two is:

$$\mathrm{RCS(dBsm)} = 10\log\left[\frac{\mathrm{RCSm}^2}{1.0\mathrm{m}^2}\right] \tag{2.2}$$

There are many factors that affect the RCS, such as scatterer structure, EM wave frequency, polarization form of incident field and scattering field, angular direction position of observer relative to the incident direction. And RCS is closely related to the frequency of incident wave and scatterer. The same target will show different characteristics of Radar Cross Section for different radar frequencies. According to the relative relationship $ka=L/\lambda$ between scatterer size L and wavelength λ, the scattering modes can be divided into low-frequency scattering mode, resonant scattering mode and high-frequency scattering mode.

(1) Low-frequency scattering mode ($ka \le 1$). In this case, the relative variation of the incident wave along the scatterer is small, so the amplitude and phase of the induced current on the target are approximately constant. In this mode, the shape change of the target is not that important.

(2) Resonant scattering mode ($1<ka<10$). In this case, when the incident wave length and the object size are much of a size, the phase change of the incident field is very significant. The field at each point on the scatterer is the superposition of the incident field and the scattered field caused by the other points on the object. The total effect of the interaction between each part of the scatterer determines the final distribution of current density.

(3) High-frequency scattering mode ($ka \ge 10$). In this case, the scattered field has a special correlation with the incident angle. High frequency scattering is a local phenomenon, and the total scattering field of the target can be obtained by the superposition of the scattering fields of each independent scattering center, which makes the detailed geometric results in the scattering process very important, and the peak of the scattering level is mainly related to some isolated points.

Because the RCS of the target is not only a function of the incident angle of the radar signal, but also a function of the azimuth of the receiver, it can be divided into single station and double station [36]. When the transmitter and receiver are not at the same point, it is called bistatic scattering. Generally speaking, forward scattering is the case when the bistatic angle is 180°, while the monostatic scattering means the bistatic angle is 0°.

2.1.2 PO Algorithm for PEC

The basic principle of the PO algorithm is based on the Stratton-Chu equation, and the scattering field is obtained by analyzing the surface current of the target [37]. According to the principle of locality, the influence of induced current on each part of the surface is ignored during calculation, and the induced current is represented by the incident field approximately.

When using PO algorithm to solve the induced current on the object surface, there are three basic assumptions:

(1) The curvature radius of the target surface is much larger than the wavelength, which means that the target is electrically large.

(2) The induced current only exists in the region illuminated by the incident wave, no induced current distribution in the shadow region.

(3) The induced current distribution on the target surface is consistent with that on the infinite tangent plane.

PO algorithm is based on the above three important assumptions, it is a high-frequency algorithm based on approximate assumptions, so some calculation accuracy is sacrificed [37]. For targets with complex structure, the accuracy of the algorithm is difficult to be guaranteed, but it improves the calculation efficiency and the calculation range of electrical size. Therefore, it can be widely used in the scattering calculation of high-frequency electrically large targets.

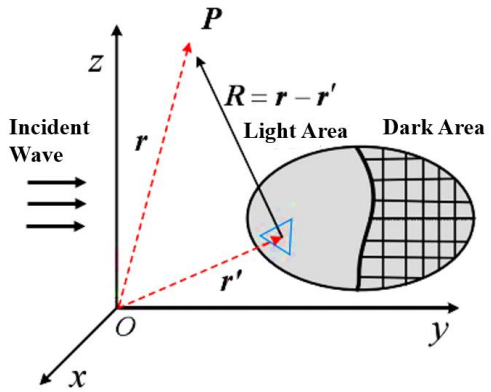

Fig. 2.1 Schematic diagram of PEC target for PO algorithm

Considering a PEC target, as is shown in Fig. 2.1, the magnetic vector potential generated by the induced current distribution $\boldsymbol{J}_s$ on the target surface at the field point P [39] can be expressed as

$$\boldsymbol{A}(\boldsymbol{r}) = \frac{\mu}{4\pi}\iint_s \frac{\boldsymbol{J}_s(\boldsymbol{r}')e^{-jkR}}{R}ds' \tag{2.3}$$

Where R=| $\boldsymbol{r}$ - $\boldsymbol{r}'$|, $\boldsymbol{r}'$ is the source position vector, $\boldsymbol{r}$ is the observer position vector, $\boldsymbol{J}_s(\boldsymbol{r}')$ is the induced current density at position $\boldsymbol{r}'$ on the target surface, and ds' is the element area at $\boldsymbol{r}'$.

Since the radar cross section is a far-field calculation, $kR \gg 1$, the corresponding equations of magnetic field and electric field can be obtained from equation (2.3)

$$\boldsymbol{H} = \frac{1}{4\pi}\iint_s \frac{-1-jkR}{R^3} e^{-jkR}\left[\boldsymbol{R}\times\boldsymbol{J}_s(\boldsymbol{r}')\right]ds' \tag{2.4}$$

$$\boldsymbol{E} = \frac{-k^2}{j\omega\varepsilon\cdot 4\pi}\iint_s \frac{e^{-jkR}}{R}\hat{R}\times(\hat{R}\times\boldsymbol{J}_s(\boldsymbol{r}'))ds' \tag{2.5}$$

Where $\hat{R} = \boldsymbol{R}/|\boldsymbol{R}|$.

For PEC scatterer, the induced current distribution on the surface is approximately obtained by PO algorithm

$$\boldsymbol{J}_s(\boldsymbol{r}') = \begin{cases} 2\hat{n}(\boldsymbol{r}')\times\boldsymbol{H}^i(\boldsymbol{r}'), & \boldsymbol{r}' \in Bright\ Region \\ 0, & \boldsymbol{r}' \in Shadow\ Region \end{cases} \tag{2.6}$$

Where $\boldsymbol{H}^i(\boldsymbol{r}')$ is the incident magnetic field at the surface $\boldsymbol{r}'$ assuming that the scatterer does not exist, $\hat{n}$ is the panel normal unit vector at position $\boldsymbol{r}'$.

Substituting equation (2.6) into equation (2.5), it can be obtained that the far-field scattering field of physical optics is:

$$\boldsymbol{E}^s(\boldsymbol{r}) = \frac{-k^2}{j\omega\varepsilon\cdot 2\pi}\iint_{s_l} \frac{e^{-jkR}}{R}\hat{R}\times[\hat{R}\times(\hat{n}\times\boldsymbol{H}^i)]ds_l \tag{2.7}$$

Where S_l represents the bright region of the object, k is the wave vector, $k = |\boldsymbol{k}| = 2\pi/\lambda$.

In general, the radar is far from the scatterer, so the plane wave approximation is usually used to calculate the RCS, and the expression of the incident field is:

$$\boldsymbol{E}^i(\boldsymbol{r}') = \boldsymbol{E}_0 e^{-j\boldsymbol{k}\cdot\boldsymbol{r}'} = \hat{x}e^{-jk\hat{z}\cdot\boldsymbol{r}'} \tag{2.8}$$

$$\boldsymbol{H}^i(\boldsymbol{r}') = \frac{1}{\eta}\hat{k}\times\boldsymbol{E}^i(\boldsymbol{r}') \tag{2.9}$$

In the far-field case, there can be the following approximation:

$$\begin{cases} R = |\boldsymbol{r}-\boldsymbol{r}'| \approx r - \hat{r}\cdot\boldsymbol{r}' \\ R \approx r \end{cases} \tag{2.10}$$

By substituting equations (2.8) to (2.10) into equation (2.7), the scattered field expression is

$$\boldsymbol{E}^s(\boldsymbol{r}) = \frac{j}{\lambda r}|\boldsymbol{E}_0|e^{-jkr}\boldsymbol{I} \tag{2.11}$$

$$\boldsymbol{I} = \iint_{s_l} \hat{r}\times\left\{\hat{r}\times\left[\left(\hat{n}(\boldsymbol{r}')\cdot\hat{E}_0\right)\hat{k} - \left(\hat{n}(\boldsymbol{r}')\cdot\hat{k}\right)\hat{E}_0\right]\right\}e^{-jk(-\hat{r}+\hat{k})\boldsymbol{r}'}ds_l \tag{2.12}$$

According to the definition of RCS, the PO expression of RCS is

$$\sigma = \lim_{R\to\infty} 4\pi R^2 \frac{\left|\boldsymbol{E}^s\right|^2}{\left|\boldsymbol{E}^i\right|^2} = \frac{4\pi}{\lambda^2} |\boldsymbol{I}|^2 \tag{2.13}$$

Therefore, RCS can be obtained by calculating $\boldsymbol{I}$.

2.1.3 Verification of PO Algorithm for PEC

Now we use FEKO software to verify the correctness of the PO algorithm. As is shown in Fig. 2.2, we choose the hemisphere shell with 1m radius as the model. Here are the parameters we set in FEKO, the incident wave frequency is 1GHz, the incident angle is θ_i =180°, φ_i = 0°, the scattering angle is θ_s = [0°,180°], φ_s = 0 °, the material of the hemisphere is PEC, the partition size is 1λ. Compared with the RCS of PEC target calculated by FEKO's PO algorithm, as is shown in Fig. 2.3, the red solid line represents the bistatic RCS results calculated by FEKO software, and the blue dotted line represents the calculation results of the equations in Section 2.1.2.

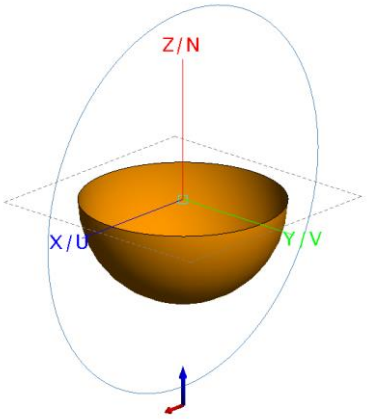

Fig. 2.2 Hemisphere shell model in FEKO

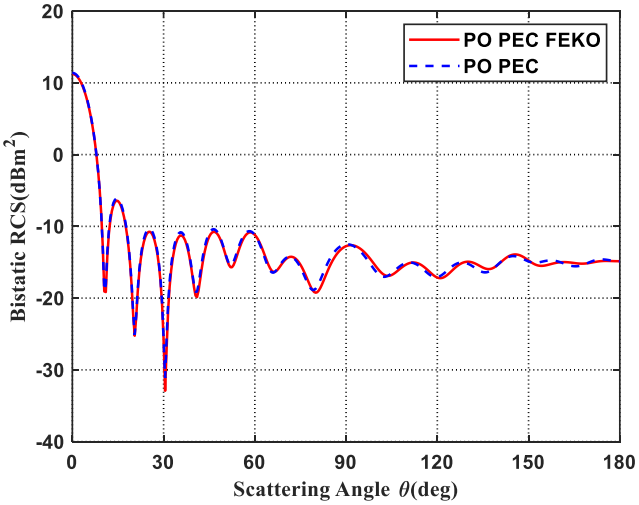

Fig. 2.3 Bistatic RCS comparison for hemisphere shell

For the PEC hemisphere shell model, the RCS even error between FEKO and our thesis can reach 0.3426dB, which is enough to verify the correctness of our PO algorithm derivation.
For the hemisphere shell target shown in Figure 2.2, when the plane wave irradiates from the bottom, the outside of the whole hemispherical shell is illuminated, so there is no problem of judging the bright and shadow region. However, for other complex targets, there will be bright and shadow region when illuminated by plane wave or point source.

2.2 Basics of UI Software System

We use the Qt5 as the platform to develop the Occlusion judgement UI software system. For the occlusion judgement of the model, the most intuitive result is the visual graphics, so we developed a visual window based on OpenGL Application Programming Interface (API).

2.2.1 Qt Platform Introduction

Qt is a cross platform graphical user interface application framework based on C++ language. It is not a programming language, but a framework written in C++, which can develop all kinds of applications. Qt has its own Integrated Development Environment (IDE), called Qt Creator, it is designed specifically to support cross platform application development, and can ensure that software developers who have not been exposed to Qt framework can quickly get familiar with and operate. It runs on Linux, OSX and Windows, and provides intelligent code completion, syntax highlighting, integration help system, debugger and analyzer integration.
In this thesis, Qt is used to develop the UI software system, which has the following advantages.
(1) Excellent cross platform characteristics
Qt Creator supports some mainstream operating systems, such as Windows and Linux. The API provided by Qt supports all platforms, the programs developed by programmers using API in one system can be easily transplanted to others without considering the compatibility of the system.
(2) Fully object-oriented
Qt is based on C/C++ programming language. Users can use the object-oriented characteristics of C++ to design the developed system and encapsulate the developed functions.
(3) Rich application program interface
Qt contains many C++ class libraries, including file processing, multithreading development and I/O device management. Qt also includes OpenGL class library, which supports the rendering of 2D/3D graphics. Even more, Qt contains regular expression libraries.

2.2.2 OpenGL API Introduction

OpenGL (Open Graphics Library) as the industrial standard of 3D graphical software interface, is independent of hardware and software operating system. It can be implemented on different systems, such as Windows and Linux. It can be closely interfaced with various programming languages to facilitate the design of relevant graphics rendering algorithms. OpenGL is easy to use and efficient, it has several functional modules, such as modeling, transformation, bitmap display, image enhancement, texture mapping and so on.

The occlusion judgement system developed in this thesis is based on Qt platform, and OpenGL is used to display the model and occlusion judgement result in Qt application. It is mainly based on the following advantages of OpenGL: (1) An OpenGL component class is provided, which can be used like other Qt components, simplifying the development of application programs. (2) OpenGL graphics rendering commands are independent of Windows. (3) OpenGL has good portability. (4) The strong openness allows OpenGL to carry out secondary development and realize high-performance 3D graphics simulation.

The basic steps of rendering 3D graphics on the computer screen are as follows:

(1) The model is established according to the basic graphics unit (point, line, bitmap and image are called basic graphics unit in OpenGL), and the established model is described by mathematical equation.

(2) Put the model in the appropriate position in the 3D coordinate space, and set the viewpoint to observe the model.

(3) The mathematical description of the model and its color information are converted into pixels on the computer screen by graphic code and displayed in the window.

2.2.3 Occlusion Judgement Software Introduction

For the occlusion judgement software, here are five main parts, as is shown in Fig. 2.4. The process of the whole operation is showing in Fig. 2.5.

(1) Import file part

This software can import and recognize two main mesh file types, **.dat* and **.nas* format file. **.dat* file contains the vertex and patch information of quadric surface, and it is generated by Altair Hypermesh, while **.nas* file contains the triangular path information and it is generated by Altair Feko. Here we can click the Open button and choose the required file under the file path, and the path and file name will display in the text box.

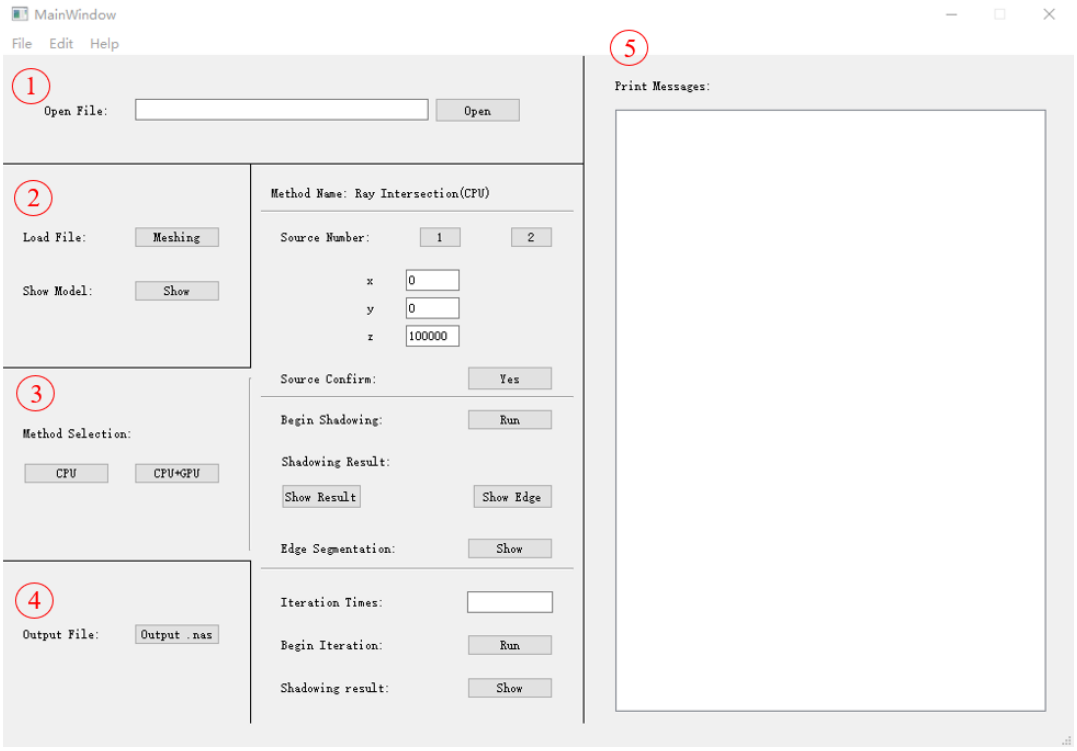

Fig. 2.4 Interface of the occlusion judgement software

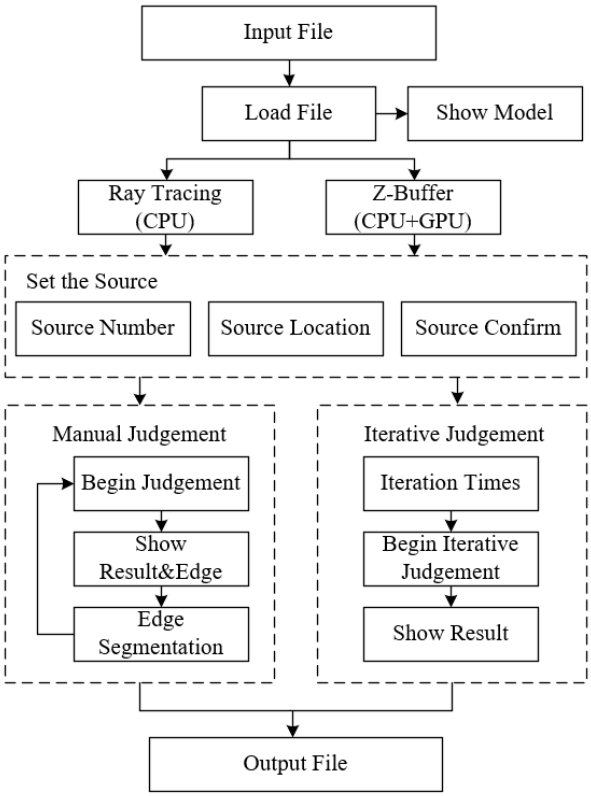

Fig. 2.5 The process of UI interface operation

(2) Load file and show model

After selecting the required file, we need to read the node information of the meshed model, the corresponding operation is clicking the Meshing button. In the process of loading file, firstly

we read the number of vertices and patches of the quadric surface or triangular patch, then we read the vertex coordinates and patch index according to the number of vertices and patches, and store these data in global variables for later processing. After reading information, the **.dat* will be converted into quadrilateral patch **.quadfacet* file and triangular patch **.trifacet* file for easy output and utilization, the **.nas* file will be converted to **.trifacet* file directly.

After loading the file, we can click the Show button in part 2 to visualize the model in OpenGL widget. We select the F35 target as the model whose length, width and height are 35m * 30m * 4m respectively. Here, we use the blue patch to represent the original model, the total patch num is 3396, as shown in Fig. 2.6.

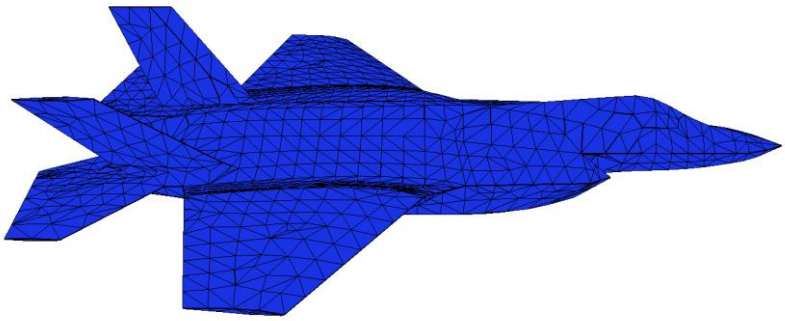

Fig. 2.6 F35 model displayed by OpenGL widget

(3) Select method and begin occlusion judgement

In this part, we need to select an appropriate method to judge the bright region. Here CPU button represents ray tracing method while CPU+GPU button represents the Z-Buffer method. We will compare the advantages and disadvantages of these two methods in the following sections. After selecting the method, we need to set the source number and the source position. At present, we can select one or two sources, then set the location of each source, and finally confirm the source setting. Then we judge the bright region patch, show the bright region result and find the edge of the bright region and shadow region, finally we can segment the edge patch. For the manual part, we can judge the bright region again after remeshing. For the iterative part, we can set the number of iterations to reduce the amount of manual operation.

(4) Output file

At present, the software system only has the occlusion judgement part, so it is necessary to export the vertex information and patch index information of the bright region for PO algorithm. The exported file format is **lit.nas*.

(5) Print message box

The print message box interacts with users by printing messages such as the operation name, the vertex number, the patch number and the total computation time.

2.3 Occlusion Judgement

2.3.1 Ray Tracing Method

Ray tracing method is a traditional occlusion judgement method based on CPU. Judging whether the patch can be illuminated by the incident wave is divided into two steps. First, judge whether the patch is shadowed by itself. If the patch is shadowed by itself, we judge the next patch. Otherwise, judge whether the patch is shadowed by other patches.

(1) Self-occlusion

For self-occlusion case, the basic idea is, first take the normal vector direction of its illumination surface, multiply it by the incident wave direction vector, and judge whether it is occluded according to the obtained results. In the case of plane wave incidence, as shown in Fig. 2.7(a), if the angle between the normal $\hat{n}$ of the patch and the incident wave direction $\hat{k}_i$ is $\alpha > 90^\circ$, that is, $\hat{n} \cdot \hat{k}_i < 0$, the patch is illuminated, and if $\alpha < 90^\circ$, the patch is blocked. For the point source case, as shown in Fig. 2.7(b), the direction from the source point to the center point of the triangular patch is regarded as the incident wave direction $\hat{k}_i$ in the case of plane wave, and the judgement method is similar to that of plane wave.

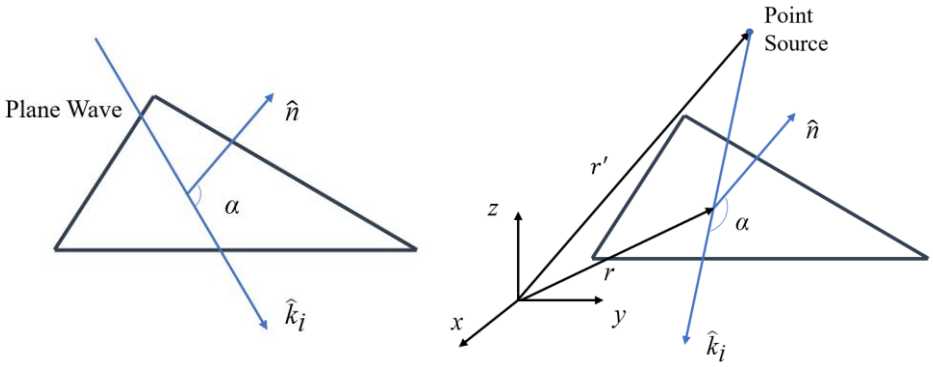

(a) Plane wave (b) Point source

Fig. 2.7 The diagram of self-occlusion

(2) Mutual occlusion

The occlusion under the illumination of point source is shown in the Fig. 2.8. Patch 1 represents the patch to be occluded, Q is the center point on Patch 1, Patch 2 represents any patch, P is the point source of the incident wave. The criterion to judge occlusion is that if the center Q of the patch is shadowed by other patches, the patch is shadowed by the incident wave, otherwise, it is illuminated by the incident wave.

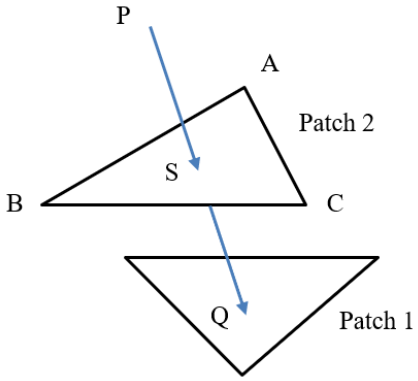

Fig. 2.8 The diagram of mutual occlusion

The algorithm used here is: if there is a line between the source point P and the center point Q of the current patch, the direction P to Q is the direction of the incoming wave. If there are any intersections, the current patch is considered to be covered.

Suppose that the three vertices of any patch of the scatterer are A, B, C, the point source is P, and the central point of the patch to be occluded is Q. Using the parametric equation, any point on the patch M can be expressed as:

$$S = \alpha A + \beta B + (1 - \alpha - \beta)C \tag{2.14}$$

Where α, β, $\gamma = (1 - \alpha - \beta)$ are the area coordinates. If α, β and γ are all in the interval [0,1], then the point S is inside the triangle, otherwise it is outside. The coordinates of any point on the line segment PQ are:

$$S = \lambda P + (1 - \lambda)Q \tag{2.15}$$

Where λ is the distance from point S to Q. If λ is in the interval [0,1], it means that the point is on the line segment, otherwise it is not. If point S is on both line segment PQ and Patch 1, then S is the intersection of line segment PQ and Patch 1, we have:

$$\alpha(A - C) + \beta(B - C) + \lambda(Q - P) = Q - C \tag{2.16}$$

That is

$$\alpha(\boldsymbol{CA}) + \beta(\boldsymbol{CB}) + \lambda(\boldsymbol{PQ}) = \boldsymbol{CQ} \tag{2.17}$$

Write it as a matrix

$$[\boldsymbol{CA}\ \boldsymbol{CB}\ \boldsymbol{PQ}]\begin{bmatrix}\alpha\\ \beta\\ \lambda\end{bmatrix} = [\boldsymbol{CQ}] \tag{2.18}$$

If $\det[\boldsymbol{CA}\ \boldsymbol{CB}\ \boldsymbol{PQ}] = 0$, then there is no solution to this equation, which means there is no intersection between PQ and Patch 2, Patch 1 is not be shadowed. Otherwise, there is intersection between PQ and Patch 2. When α, β, γ, λ are all in the interval [0, 1], the patch is

shadowed. When any one of α, β, γ, λ is not in the interval [0, 1], the patch is illuminated. The specific flow of the algorithm is shown in Fig. 2.9.

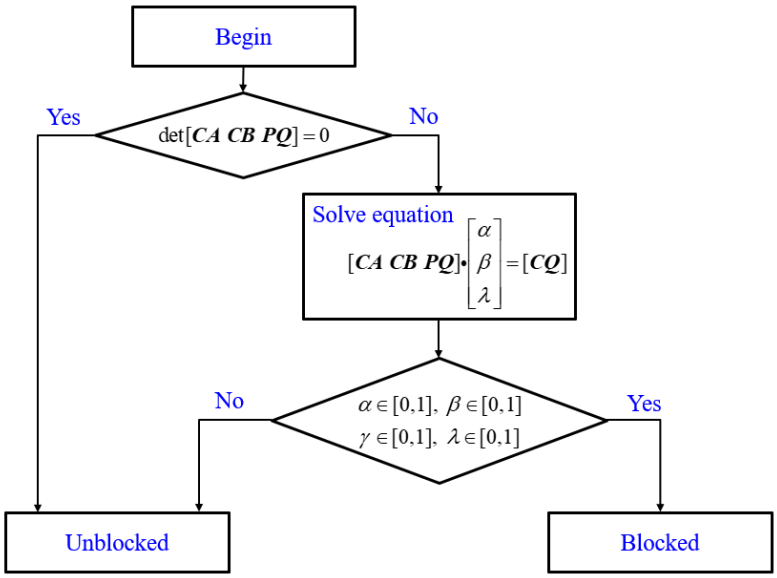

Fig. 2.9 Program framework of ray tracing method

After occlusion judgement, the edges of the model will be sawtooth. The reason is when judging the patch, it only depends on whether the center of the patch is irradiated by the incident wave. If the center point is irradiated, the patch is illuminated, otherwise it is shadowed. This aliasing will bring some errors to the occlusion judgement, we will propose a method based on edge patch segmentation to reduce this kind of error in the Section 2.4.

2.3.2 Z-Buffer Method

Using GPU's shader and depth buffer can realize fast occlusion judgement. The current GPU supports programmable vertex shaders to perform vertex level operations, and supports fragment shaders to perform fragment level operations [40]. Vertex data is used as input to the graphics rendering pipeline, as shown in Fig 2.10. Vertex shaders will process vertex data in the order of vertices entering the pipeline. A fragment in OpenGL is all the data that OpenGL needs to render a pixel.

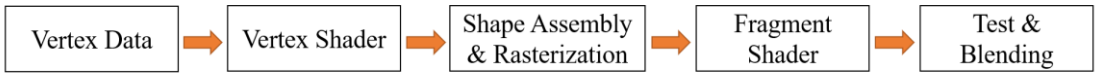

Fig. 2.10 Graphical rendering pipeline diagram

The whole OpenGL process is as follows. Firstly, read the vertex data, then change all vertex coordinates from the world coordinate system to the local coordinate system, and determine the attributes of the vertices, then form the transformed vertices into primitives (line segments,

triangles, polygons) according to the instruction information, and transform the pixels, which will produce obvious bright and shadow region. Then rasterize the primitives in the bright region, that is, corresponding to the screen pixels, and finally store all the information in the cache for rendering.

When drawing a 3D patch onto a 2D screen, it is equivalent to projecting the 3D coordinate information onto the 2D screen, and the patch will be discretized into pixels. GPU will record two attributes of screen pixels, color value (frame cache) and depth value (Z-Buffer [41][42][44]) from the projection screen. The computer screen is equivalent to the observation position. Compared with the screen, the near target will block the far target, and the depth value of the near target is less than that of the far target. The pixel of the screen will only retain the information of the nearest patch, and the far patch information will give up. As shown in Fig. 2.11, the viewing direction is *-z* direction, and the object in the box will be projected to the near plane, so with the Z-Buffer technology, the patch displayed in the near plane is the bright region patch.

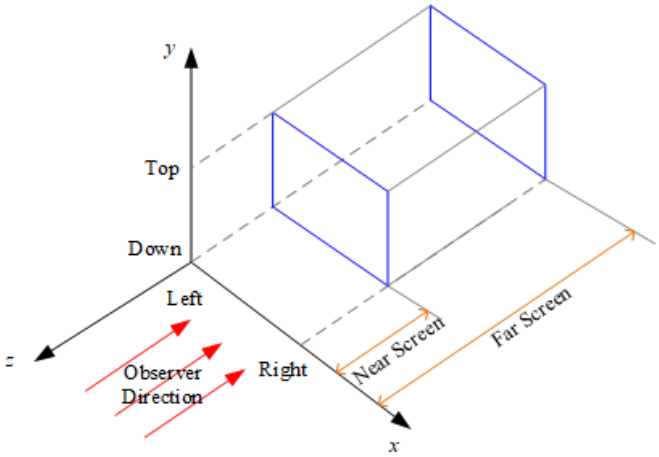

Fig. 2.11 Plane wave incidence corresponding to orthophoto projection

The whole occlusion judgement process of Z-Buffer is as follows [45].

1) Before painting, the frame cache and depth cache of screen pixels are cleared (white) and placed at infinity respectively.

2) According to the input sequence, assign a specific color to each patch as a mark. The total number of colors that can be combined by 8-bit RGB is $(2^8)^3$, in which one color (white) is selected as the background, so the total number of colors that can be used is 16777215, and the color allocation relationship is as follows

$$C_i = \frac{\left[\left(2^8\right)^3 - 1\right] i}{N} \tag{2.19}$$

Where i is the patch serial number, N is the total number of patches, and C_i is the color of the i th patch.

3) The depth value of the patch is calculated according to the projection matrix. Before drawing each patch, compare the depth value of the patch with the original depth value of the pixel. If the original depth value of the pixel is greater than the patch depth value, this means the new patch is closer, so the color value of the current patch is stored in the frame cache of the pixel. On the contrary, the pixel frame cache at the corresponding position will not modified.

4) After all patch are operated, read out the pixel color that can be drawn on the screen, and obtain the number of facets according to equation (2.19), so as to extract the bright region patch. Select a complex aircraft model F35, as is shown in Fig. 2.6. The plane wave incident direction is vertical incident from the top ($\theta = 0^\circ, \varphi = 0^\circ$). After assigning different colors to the patches according to the patch number, project the 3D target onto the 2D screen, as shown in Fig. 2.12.

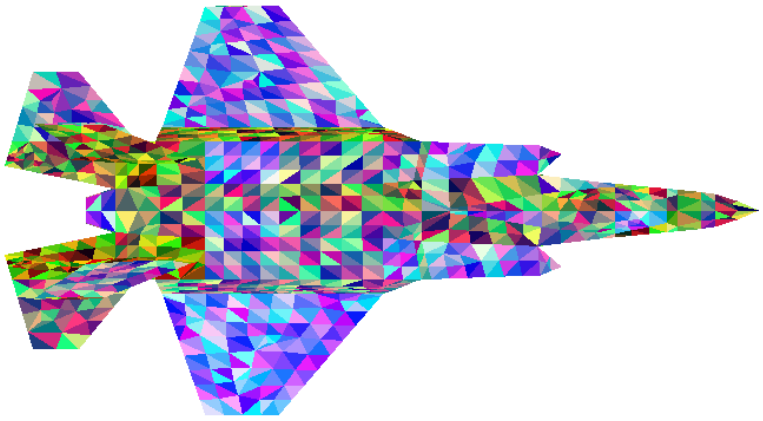

Fig. 2.12 Plane projection results

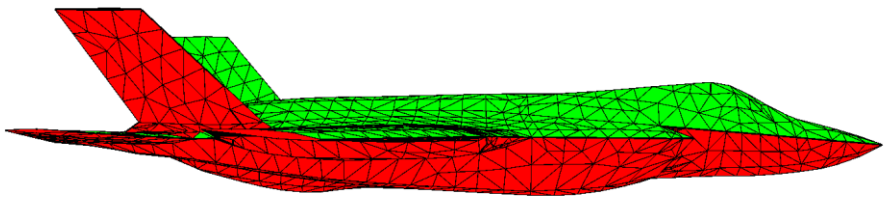

Fig. 2.13 Final bright region output result

Finally, the brightness of the patch is judged by reading the color on the 2D screen. The final result found by Z-Buffer is shown in Fig. 2.13. We use green color to represent the bright region, while the red color region represents the shadow region. By assigning a unique color to the patch for marking, this method can restore the information of the patch according to its unique color value. However, when a patch is only partially occluded, the non-occluded part will also appear on the screen. When GPU read the pixels, the corresponding color will be read, and GPU

believe that the whole patch is in the bright region, which will introduce some errors. We will discuss how to reduce this kind of error in the next section.

2.4 Edge Patch Segmentation

2.4.1 Process of Edge Patch Segmentation

When we judging the bright region of the scatterer, there are errors in the edge patch between the bright region and the shadow region for both two methods. The difference is that there are errors for ray tracing method in both bright and shadow region edge patch, while the error of Z-Buffer method only exists at the edge of the bright region. And the reason we have explained in Section 2.3. Therefore, for more accurate occlusion judgement result, we need to further segment and judge the edge patches of bright and shadow region.

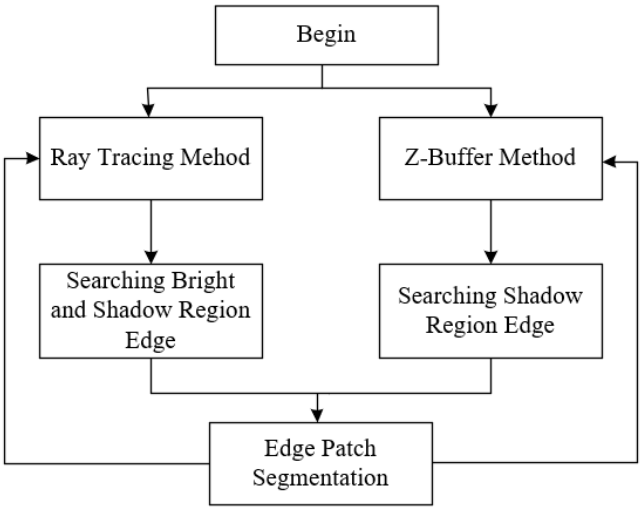

Fig. 2.14 Progress of edge patch segmentation method

The edge patch segmentation method of occlusion judgement process is shown in Fig. 2.14. This method needs to determine the edge patch first. The general idea of determine bright region edge patch is to traverse the vertices of the bright triangle patch. If this vertex exists in the vertex set of the shadow triangle patches, then we can determine that this triangle patch is an edge triangle patch. As is shown in Fig. 2.15 (a) and (b), the green color region means the bright region, the yellow color means the edge bright region, the red color means the shadow region, the blue color means the edge shadow region.

Then the next step is to segment the edge triangle patches. The segment rule is finding the center of the triangle and the trisection points of the three sides, and then reorganizing these points into 9 new triangles. As we can also see from Fig. 2.15 (a) and (b), the patch size in the edge region is 1/9 of the center region. After further edge mesh segmentation, we can judge the bright

region of the new parches in an iterative way, in this way a sufficiently accurate judgement result can be obtained.

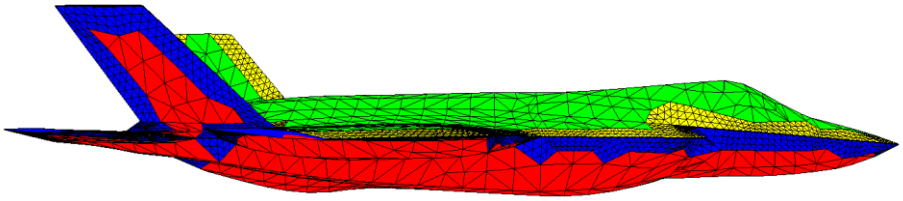

(a) Ray tracing method

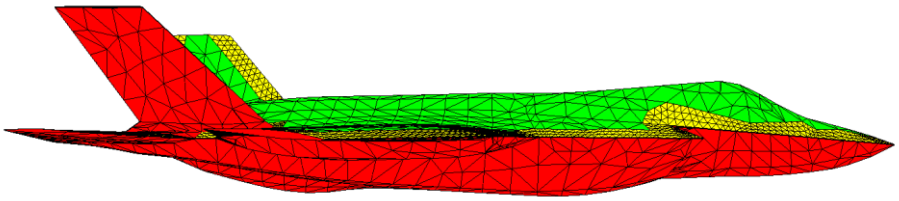

(b) The Z-Buffer method

Fig. 2.15 The edge patch segmentation result of two methods

2.4.2 Edge Patch Segmentation Method Verification

Due to the F35 aircraft target is too complicated, here we use a simple sphere plate model to verify the results of occlusion judgement more intuitively. The upper part of the model is a sphere with 1m radius, and the lower part is a square with 4m side length, the height between the spere center and the plate is 2m. After the first model division in Hypermesh software, the number of triangular patches is 1540. We use a plane wave with an incidence angle of $\theta = 0°$ and $\varphi = 0°$, that means it is incident from the upper part of the model, and the first judgement result of the bright region is shown in Fig. 2.16.

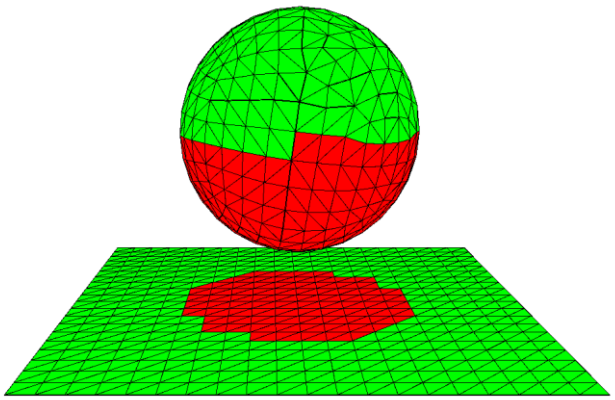

Fig. 2.16 First judge result for sphere pad Model

Here we take the projection of the sphere on the plate, as is shown in Fig. 2.17 (a). Due to the oversize patches, the projection result looks like a polygon rather than a circle. Fig. 2.17 (b) and (c) are taken from the yellow dotted box in Fig. 2.17 (a), indicate the fourth iteration results of ray tracing method and Z-Buffer method respectively. It can be seen that due to the segmentation of edge patches, the shadow region edge in both results appear more round, and there are four sizes of triangles due to the edge patch is divided three times. Through further observation, there are some errors in Z-Buffer technology, the bright and shadow patches are arranged cross at the edge part, which will be explained in the next section.

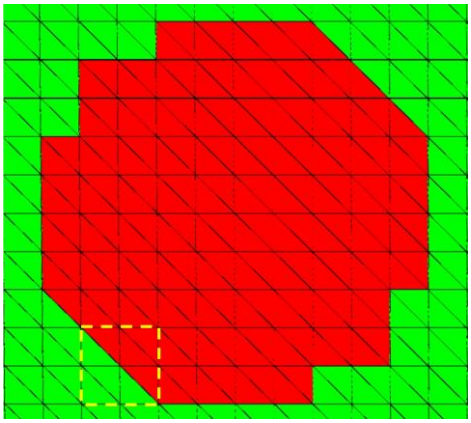

(a) The first occlusion judgement result

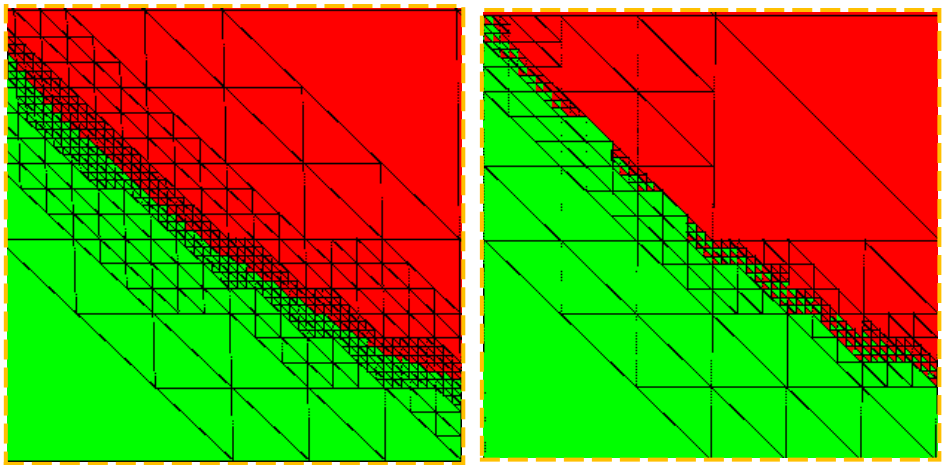

(b) Ray Intersection result (c) Z-Buffer result

Fig. 2.17 The occlusion judgement result on the pad

Table 2.1 shows the comparison of two methods on the patch number and time consuming for each iteration time. With the increase of the iteration time, the patch number of ray tracing method is more than that of the Z-Buffer method, and the time consumption is also higher than that of the Z-Buffer method. Due to ray tracing method needs to segment the patches at the bright and shadow region edge, while Z-Buffer method just segment the patches at the bright region, so the patch number of Z-Buffer method is more than that of the Z-buffer method.

Moreover, the time-consuming of ray tracing method is much more than that of Z-Buffer method, because the time complexity of ray tracing method is O (N^2). While the Z-Buffer method based on GPU rendering principle which greatly reduces the time and memory consumption, and its algorithm complexity depends on the resolution of the screen rather than the number of patches, which can be considered as O (N). In fact, the rendering pipeline of GPU is parallel and the actual processing speed is faster. The device parameters used in this thesis are Intel (R) core (TM) i5-10400 processor, 2.9 GHz clock frequency, Intel(R) UHD Graphics 630 display adapter.

Table 2.1 Comparison of ray tracing method and Z-Buffer method

Iteration Time	Ray tracing method		The Z-Buffer method	
	Patch Number	Time Cost	Patch Number	Time Cost
1th	1540	0.925s	1540	0.013s
2th	3780	4.418s	2692	0.056s
3th	10708	32.166s	5716	0.097s
4th	31784	268.395s	17092	0.141s

2.4.3 Error Analysis

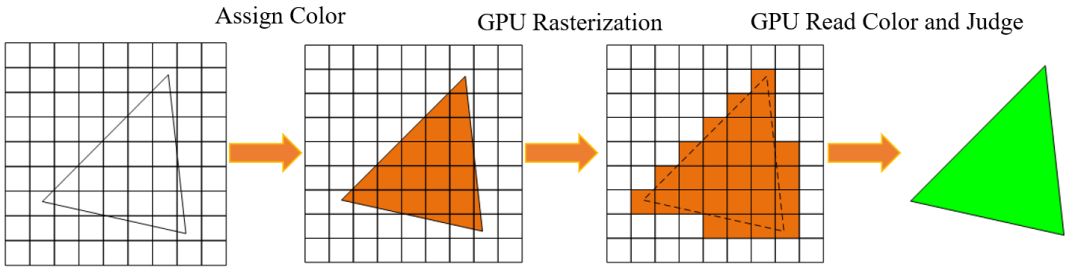

(a) Case 1: Patch size larger than pixel size

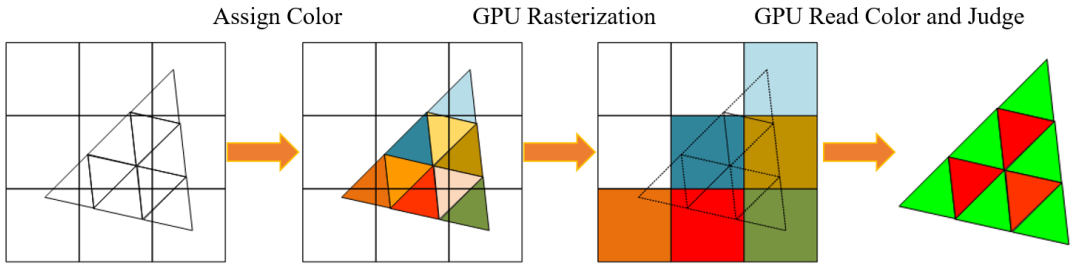

(b) Case 2: Patch size smaller than pixel size

Fig. 2.18 Error analysis for Z-Buffer method

In Fig. 2.17(c), the bright and shadow patches are arranged cross at the edge region. When the edge patch is continuously segmented to a certain time, there will be two kinds of patches. The

first one is the patch size larger than the pixel size. In this case, as is shown in Fig. 2.18(a), Z-Buffer method will not make the above mistake. However, when the edge patch is segmented to a certain size, as shown in Fig. 2.18(b), there are 9 triangular patches in the 3×3 pixels screen, and the size of the triangular patch is smaller than the pixel points. After assigning colors to each patch, the graphics will be displayed in the form of pixels by rasterization. In this step, some colors will be lost resulting in some triangles being judged as shadow patches. The above is the main reason for the error of Z-Buffer method. At present, the solution is to use better screen and display adapter or use multiple screens to operate together.

2.5 Chapter Summary

In this chapter, we first introduce the concept of RCS and the PO algorithm for PEC. Then we briefly introduce QT, OpenGL, and the occlusion judgement software system based on QT and OpenGL. Then two methods for occlusion judgement are introduced, namely ray tracing method and Z-Buffer method. To improve the occlusion judgement result, we segment the edge of bright and shadow region, and then judge the patched again. However, when using Z-Buffer method, some new errors will be brought after a certain times segmentation, and we have explained the reasons of this kind of errors.

3 Scattering Characteristics of Hypersonic Vehicle Covered by Plasma Sheath

When we study the EM scattering characteristics of the plasma sheath covered vehicle, we can regard the plasma sheath as a special coating medium covering the vehicle surface. The vehicle itself is made of PEC, and the medium coated on its surface can be layered according to the plasma sheath electron number density, so as to achieve more accurate modeling. For this kind of electrically large composite object, we use the PO algorithm in high frequency method to solve the EM scattering characteristics of the plasma sheath coated target.

In order to study the impact of plasma sheath on RCS, there are three methods, flight test, ground test and numerical simulation. Flight test can only measure one set of data at a time, which is expensive and time-consuming. Wind tunnel is generally used to simulate the real flow field of reentry body in ground experiment, which is expensive and difficult to restore. With the development of computer and related commercial software, numerical simulation has become a feasible way of flow field calculation.

In this chapter, we will introduce PO algorithm for coated object at first. Then we use the CFD-FASTAN to simulate the flow field around the hypersonic vehicle. Therefore, we need to introduce the basic flow field knowledge of CFD-FASTRAN before simulation. Next the plasma sheath is modeled as layered model after the electron number density data is obtained. Finally, we compare the Radar Cross Section of plasma sheath coated targets at different flight heights and speeds.

3.1 PO Algorithm for Coated Targets

3.1.1 PO Algorithm with Step Method

Consider that there is plane wave and a plasma sheath coated vehicle in the space, as shown in Fig. 3.1 [36].

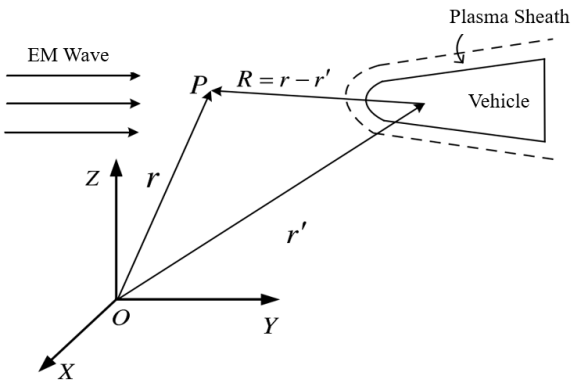

Fig. 3.1 Schematic diagram of coating target

After the far field approximation, in the case of plane wave incidence, the scattered field at an external point can be calculated by the following equation

$$\boldsymbol{E}^s = \frac{-jk}{4\pi}\frac{\exp(-jkr)}{r}\int_{s_l}\hat{R}\times\left[\hat{n}\times\boldsymbol{E}^T-\eta\hat{R}\times\left(\hat{n}\times\boldsymbol{H}^T\right)\right]\exp\left(jk\hat{R}\cdot\boldsymbol{r}'\right)ds_l \tag{3.1}$$

Where k and η are the wave number and intrinsic impedance of free space respectively, $\hat{R}$ is the unit vector of scattered wave, $\boldsymbol{r}$ is the position vector of point P, $r = |\boldsymbol{r}|$, $\hat{n}$ is the unit normal vector outward from the surface. $\boldsymbol{E}$ and $\boldsymbol{H}$ are the total electric field and total magnetic field on the boundary respectively, they are composed of incident component and scattering component.

$$\begin{cases}\boldsymbol{E}^T = \boldsymbol{E}^i + \boldsymbol{E}^s \\ \boldsymbol{H}^T = \boldsymbol{H}^i + \boldsymbol{H}^s\end{cases} \tag{3.2}$$

Where, $\boldsymbol{E}^i$ and $\boldsymbol{H}^i$ are incident electric field and incident magnetic field on the boundary respectively, $\boldsymbol{E}^s$ and $\boldsymbol{H}^s$ are scattered electric field and scattered magnetic field on the boundary respectively. Here we introduce the local coordinate system, and the scattering diagram of the medium surface is shown in Fig. 3.2.

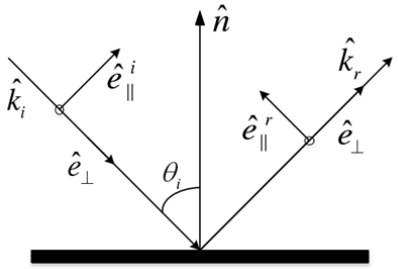

Fig. 3.2 Local coordinate system on the target surface

In Fig. 3.2, θ_i is the incident angle, the vectors $\hat{\mathrm{e}}_{//}^{i}$ and $\hat{e}_{//}^{r}$ are the polarization direction of the incident electric field and the reflected electric field parallel to the incident plane respectively, and the vector $\hat{e}_{\perp}$ is the polarization direction of the incident electric field and the reflected electric field perpendicular to the incident plane. They have the following relationships

$$\hat{e}_{\perp} = \frac{\hat{k}_i\times\hat{n}}{\left|\hat{k}_i\times\hat{n}\right|},\ \hat{\mathrm{e}}_{//}^{i} = \hat{e}_{\perp}\times\hat{k}_i,\ \hat{e}_{//}^{r} = \hat{e}_{\perp}\times\hat{k}_r \tag{3.3}$$

Assuming that $E_{\perp}$ and $E_{//}$ are the field components of the incident electric field in the $\hat{e}_{\perp}$ and $\hat{\mathrm{e}}_{//}^{i}$ direction respectively, $R_{\perp}$ and $R_{//}$ are the reflection coefficients of the dielectric surface under vertical polarization and parallel polarization respectively, there is

$$\boldsymbol{E}^i = E_{\perp}\hat{e}_{\perp} + E_{//}\hat{e}_{//}^{i} \tag{3.4}$$

$$\boldsymbol{E}^S = R_\perp E_\perp \hat{e}_\perp + R_{//} E_{//} \hat{e}^i_{//} \tag{3.5}$$

In general, the radar is far from the scatterer, so the plane wave approximation is usually used to calculate the radar cross section, which has the following relationship

$$\boldsymbol{E}^i(\boldsymbol{r}') = \hat{e}_i E_0 e^{-jk_i \cdot \boldsymbol{r}'} \tag{3.6}$$

Then we have

$$\begin{cases} \boldsymbol{H}^i = \dfrac{1}{\eta} \hat{k}_i \times \boldsymbol{E}^i(\boldsymbol{r}') \\ \boldsymbol{H}^s = \dfrac{1}{\eta} \hat{k}_r \times \boldsymbol{E}^s(\boldsymbol{r}') \end{cases} \tag{3.7}$$

Further, we can get the equivalent electric current and magnetic current

$$\boldsymbol{J} = n \times \boldsymbol{H}^T = \frac{1}{\eta}[(1-R_\perp)E_\perp \cos\theta_i \hat{e}_\perp + E_{//}(1+R_{//})(\hat{n} \times \hat{e}_\perp)] e^{-jk\hat{k}_i \cdot \boldsymbol{r}'} \tag{3.8}$$

$$\boldsymbol{M} = -n \times \boldsymbol{E}^T = [-(1+R_\perp)E_\perp(\hat{n} \times \hat{e}_\perp) + E_{//}(1-R_{//})\cos\theta_i \hat{e}_\perp] e^{-jk\hat{k}_i \cdot \boldsymbol{r}'} \tag{3.9}$$

According to equation (3.1) to (3.9), the RCS of a coating object can be obtained by the following equation:

$$\sigma = \lim_{R\to\infty} 4\pi R^2 \frac{|\boldsymbol{E}^s|^2}{|\boldsymbol{E}^i|^2} = \frac{\pi}{\lambda^2} |\boldsymbol{I}|^2 \tag{3.10}$$

Where,

$$\begin{aligned} \boldsymbol{I} = \int_{S_l} \hat{r} \times \Big\{ & (1+R_\perp)(\hat{e}_i \cdot \hat{e}_\perp)(\hat{n} \times \hat{e}_\perp) - (1-R_{//})(\hat{e}_i \cdot \hat{e}^i_{//}) \cos\theta_i \hat{e}_\perp \\ & - \hat{r} \times \Big[(1-R_\perp)(\hat{e}_i \cdot \hat{e}_\perp)\cos\theta_i \hat{e}_\perp + (1+R_{//})(\hat{e}_i \cdot \hat{e}^i_{//})(\hat{n} \times \hat{e}_\perp) \Big] \Big\} \\ & \times \exp\Big[-ikr'(\hat{k}_i - \hat{R}) \Big] ds_l \end{aligned} \tag{3.11}$$

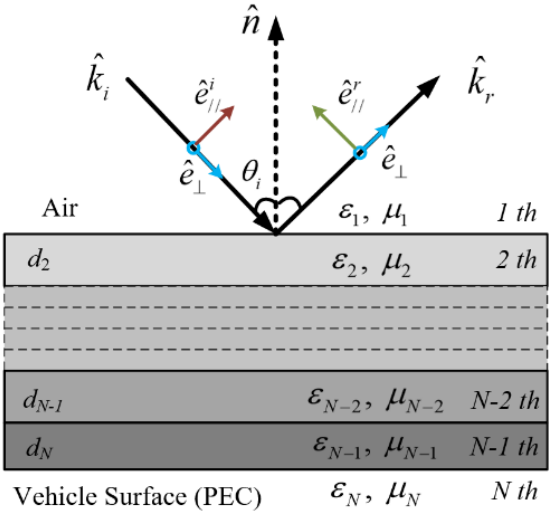

Fig. 3.3 Layered model of coated target

After the vehicle has triangular surface subdivision, nonuniform plasma is divided into multiple layers along element normal direction of every surface [46]. Plasma of every level is equivalent to uniform dielectric, as is shown in Fig. 3.3. Then, reflected coefficients of media surface are given as below [47]

$$R_{//} = \frac{Z^{(1)}\cos\theta^{(1)} - Z_{i//}^{(2)}\cos\theta^{(2)}}{Z^{(1)}\cos\theta^{(1)} + Z_{i//}^{(2)}\cos\theta^{(2)}} \tag{3.12}$$

$$R_{\perp} = \frac{-Z^{(1)}\cos\theta^{(2)} + Z_{i\perp}^{(2)}\cos\theta^{(1)}}{Z^{(1)}\cos\theta^{(2)} + Z_{i\perp}^{(2)}\cos\theta^{(1)}} \tag{3.13}$$

Where $\theta^{(n)}$ is the incident angle of EM wave in the nth layer, $Z^{(n)}$ is the media impedance of the nth layer. $Z_{i//}^{(n)}$ and $Z_{i\perp}^{(n)}$ represent input impedance of vertical and parallel polarizations of the nth layer, respectively [48], and the iterative equation is

$$Z_{i//}^{(n)} = \frac{Z_{i//}^{(n+1)}\cos\theta^{(n+1)} - iZ^{(n)}\cos\theta^{(n)}\tan\left(c^{(n)}d^{(n)}\right)}{Z^{(n)}\cos\theta^{(n)} - iZ_{i//}^{(n+1)}\cos\theta^{(n+1)}\tan\left(c^{(n)}d^{(n)}\right)} Z^{(n)} \tag{3.14}$$

$$Z_{i\perp}^{(n)} = \frac{Z_{i\perp}^{(n+1)}\cos\theta^{(n)} - iZ^{(n)}\cos\theta^{(n+1)}\tan\left(c^{(n)}d^{(n)}\right)}{Z^{(n)}\cos\theta^{(n+1)} - iZ_{i\perp}^{(n+1)}\cos\theta^{(n)}\tan\left(c^{(n)}d^{(n)}\right)} Z^{(n)} \tag{3.15}$$

Where $d^{(n)}$ is the thickness of the nth layer, and

$$c^{(n)} = k^{(n)}\cos\theta^{(n)} \tag{3.16}$$

Where,

$$\cos\theta^{(n)} = \sqrt{1 - \frac{\varepsilon_r^{(1)}\mu_r^{(1)}}{\varepsilon_r^{(n)}\mu_r^{(n)}}\sin^2\theta^{(1)}} \tag{3.17}$$

$$k^{(n)} = \omega\sqrt{\varepsilon_0\varepsilon_r^{(n)}\mu_0\mu_r^{(n)}} \tag{3.18}$$

The impedance $Z^{(n)}$ of nth layer can be expressed as

$$Z^{(n)} = \sqrt{\frac{\mu_0}{\varepsilon_0}}\sqrt{\frac{\mu_r^{(n)}}{\varepsilon_r^{(n)}}} \tag{3.19}$$

At the N th layer, we have

$$Z_{i\perp}^{(N)} = Z_{i//}^{(N)} = Z^{(N)} \tag{3.20}$$

3.1.2 Verification of PO Algorithm for Coated Targets

Here in this section, we use the same half sphere shell model with the same parameters in Section 2.2, except for the coating layer, as is shown in Fig. 2.2. In this section, the thickness

of coating layer is 5mm, the relative dielectric constant of the coating layer is ε_r = 2.6, the relative permeability is μ_r = 1.

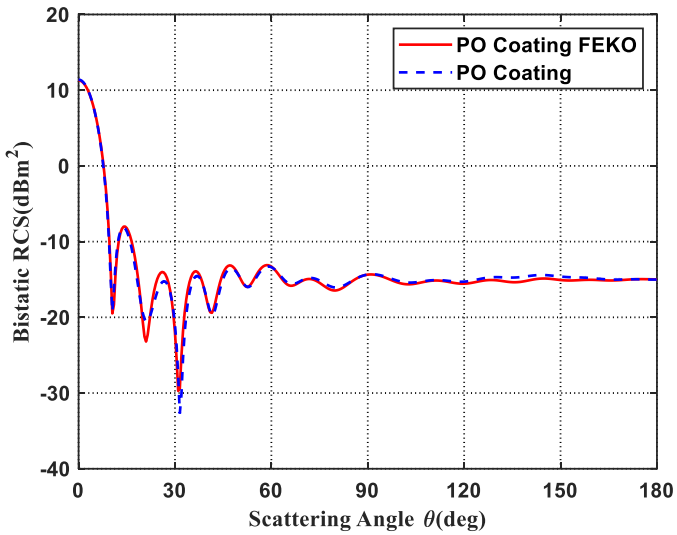

Fig. 3.4 Far field bistatic RCS for half sphere shell with coating layer

We use the step method mentioned above to get the surface reflection coefficient, and further calculate the bistatic RCS value by PO algorithm. As we can see in Fig. 3.4, the red curve represents the calculation results of the PO algorithm in FEKO, and the blue curve represents the calculation results of the PO algorithm in this thesis. The peak value of the two lines at θ_s = 0° are basically equal, and they are also basically consistent at other scattering angles, the even error of the two curves is 0.3963dB. From which we can basically determine that the PO algorithm for coating model is correct and we can apply this PO algorithm to the calculation of other models in the following sections.

3.2 Basic Parameters of Plasma

When we study the EM scattering characteristics of plasma sheath, the following parameters of plasma must be taken into account, such as plasma frequency, collision frequency, cyclotron frequency and equivalent dielectric constant.

(1) Plasma frequency

Plasma is an electrically neutral unbound macroscopic system composed of a large number of charged and neutral particles. It is the fourth state material except solid, liquid and gas. The basic parameters of non-magnetized or magnetized plasma are plasma frequency and collision frequency [49]. For magnetized plasma, another characteristic parameter is must be considered, named cyclotron frequency. In this thesis, we only consider the effect of unmagnetized plasma on Radar Cross Section.

The disturbance of charged particles in the plasma will form oscillation, and the frequency of this oscillation is the plasma frequency, which is defined as

$$\omega_p^2 = \omega_{pe}^2 + \omega_{pi}^2 \tag{3.21}$$

Where ω_{pe} is the angular frequency of plasma electron oscillation and ω_{pi} is the angular frequency of plasma ion oscillation. Their expressions are

$$\omega_{pe} = \sqrt{\frac{n_e e^2}{m_e \varepsilon_0}} \tag{3.22}$$

$$\omega_{pi} = \sqrt{\frac{n_i e^2}{m_i \varepsilon_0}} \tag{3.23}$$

Where, n_e and m_e are the electron number density and electron mass in the plasma, n_i and m_i are the ion number density and mass in the plasma, ε_0 is the vacuum dielectric constant, and e is the electron charge.

In the case of far-field scattering, the energy intensity of the incident wave is relatively weak, and the effect of the geomagnetic field on the plasma sheath can also be ignored [25]. The mass of ions is much greater than that of electrons, so the angular frequency of plasma can be approximately expressed by the angular frequency of electron oscillation as

$$\omega_p \approx \omega_{pe} = \sqrt{\frac{n_e e^2}{m_e \varepsilon_0}} \tag{3.24}$$

(2) Collision frequency

Generally speaking, plasma is mainly composed of electrons, positively charged ions and neutral particles. The plasma collision frequency can be expressed as the sum of the two collision frequencies, that is

$$\nu_{en} = \nu_m + \nu_i \tag{3.25}$$

Where ν_{en} is the effective collision frequency of electrons, ν_m is the collision frequency between electrons and ions, ν_i is the collision frequency between electrons and neutral particles, respectively.

The effective collision frequency of electrons has a great influence on the interaction between plasma and EM wave, and is an important parameter of magnetized and unmagnetized plasma. The calculation of ν_{en} needs to be determined according to the actual plasma problem, which means when the plasma generation conditions are different, the calculation equation of electron collision frequency is also different. Paper [50] show that considering the thermodynamic

nonequilibrium effect and weak ionization characteristics, the following equation can obtain high accuracy and is a relatively good choice.

$$v_{en} = 6.3\times10^{-9} n_m \sqrt{\frac{T}{300}} \tag{3.26}$$

In equation (3.26), n_m (cm^{-3}) and T represent the density of neutral particles and the temperature of plasma sheath, respectively.

(3) Cyclotron frequency

The motion of charged particles in plasma in an external magnetic field is very complex, so another basic physical quantity - cyclotron frequency needs to be used to describe the properties of magnetized plasma. The angular frequency corresponding to the electron cyclotron motion is called the electron cyclotron frequency, and its expression is [49]

$$\omega_{be} = \frac{|eB_0|}{m_e} \tag{3.27}$$

Where B_0 is the field intensity amplitude of the applied magnetic field $\boldsymbol{B}_0$.

The angular frequency corresponding to ion cyclotron motion is called ion cyclotron frequency, and its expression is [49]

$$\omega_{bi} = \frac{|eB_0|}{m_i} \tag{3.28}$$

The electron cyclotron frequency is usually used to characterize the cyclotron frequency of magnetized plasma.

(4) Equivalent dielectric constant

The interaction between plasma and EM wave is mainly expressed by its equivalent dielectric constant (dielectric tensor). For generality, the equivalent dielectric tensor of magnetized and colliding plasma in rectangular coordinate system is derived. Assuming that the applied constant magnetic flux density $\boldsymbol{B}_0$ is parallel to the z-axis, the average velocity of electrons under the action of external field is υ, and the electron number density of plasma is n_e, then the convection current density is

$$\boldsymbol{J} = -en_e\upsilon \tag{3.29}$$

The motion equation of a single electron in EM field is expanded in frequency domain

$$jm_e\omega\upsilon = -e\left(\boldsymbol{E} + \upsilon\times\boldsymbol{B}_0\right) - m_e v_{en}\upsilon \tag{3.30}$$

Where, j is the imaginary unit, ω is the angular frequency of the incident wave, m_e is the electron mass, $\boldsymbol{E}$ is the electric field intensity, and v_{en} is the electron collision frequency. For the effect

of the magnetic field intensity $\boldsymbol{H}$ on the electron is very weak compared with the external magnetic field $\boldsymbol{B}_0$, so $\boldsymbol{H}$ is ignored in the equation (3.30).

The action of plasma convection current can be equivalent to the action of dielectric tensor

$$\boldsymbol{J} + j\omega\varepsilon_0\boldsymbol{E} = j\omega\varepsilon_0\overline{\overline{\boldsymbol{\varepsilon}}}_p \cdot \boldsymbol{E} \tag{3.31}$$

Where $\overline{\overline{\boldsymbol{\varepsilon}}}_p$ is the relative dielectric tensor and can be expressed as

$$\overline{\overline{\boldsymbol{\varepsilon}}}_p = \begin{bmatrix} \varepsilon_{xx} & \varepsilon_{xy} & \varepsilon_{xz} \\ \varepsilon_{yx} & \varepsilon_{yy} & \varepsilon_{yz} \\ \varepsilon_{zx} & \varepsilon_{zy} & \varepsilon_{zz} \end{bmatrix} \tag{3.32}$$

Simultaneous equations (3.30) to (3.32) and solve them, the results are as follows

$$\varepsilon_{xz} = \varepsilon_{zx} = \varepsilon_{yz} = \varepsilon_{zy} = 0 \tag{3.33}$$

$$\varepsilon_{xx} = \varepsilon_{yy} = 1 + \frac{\omega_p^2\left(1 - jv_{en}/\omega\right)}{\left(j\omega + v_{en}\right)^2 + \omega_b^2} = 1 - \frac{LN}{N^2 - M^2} \tag{3.34}$$

$$\varepsilon_{xy} = -\varepsilon_{yx} = \frac{j\omega_p^2\left(\omega_b/\omega\right)}{\left(j\omega + v_{en}\right)^2 + \omega_b^2} = -j\frac{LM}{N^2 - M^2} \tag{3.35}$$

$$\varepsilon_{zz} = 1 + \frac{\omega_p^2}{j\omega\left(j\omega + v_{en}\right)} = 1 - \frac{L}{N} \tag{3.36}$$

Where, $\omega_p \approx \left(n_e e^2/m_e\varepsilon_0\right)^{1/2}$ is the plasma angular frequency, $\omega_b = \omega_{be} = \left|eB_0\right|/m_e$ is the electron cyclotron frequency, $L = \left(\omega_p/\omega\right)^2$, $M = \omega_b/\omega$, $N = 1 - jv_{en}/\omega$.

$\overline{\overline{\boldsymbol{\varepsilon}}}_p$ obtained above is the equivalent relative dielectric tensor of uniformly magnetized and colliding plasma. For plasma under other conditions, the corresponding equivalent relative dielectric tensor (constant) can be obtained by changing the variable value in equations (3.33) to (3.36). For example, for unmagnetized collision plasma, if $\omega_b = 0$ in equations (3.33) to (3.36), the equivalent relative dielectric tensor will degenerate into a scalar, and the equivalent relative dielectric constant can be expressed as

$$\varepsilon_{pr} = 1 - \frac{\omega_p^2}{\omega\left(\omega - jv_{en}\right)} = 1 - \frac{\omega_p^2}{\omega^2 + v_{en}^2} - j\frac{v_{en}}{\omega}\frac{\omega_p^2}{\omega^2 + v_{en}^2} \tag{3.37}$$

3.3 Flow Field Simulation of Plasma Sheath

In this thesis, the calculation of hypersonic chemical nonequilibrium flow is based on the commercial software CFD-FASTRAN. Various functions of the software are closely related to

the basic theory of computational fluid dynamics CFD. Before giving the simulation results, it is necessary to introduce the basic knowledge of computational fluid dynamics.

3.3.1 Temperature Model

In the thermodynamic equilibrium system, only translational energy and rotational energy of gas molecules are excited at a given pressure and temperature, various energy modes can be described by one temperature, which is the Single Temperature Model [51]. Under the condition of high temperature and high speed, the translational energy, rotational energy, vibrational energy and electronic energy of gas molecules are excited, and the gas is in a thermodynamic non-equilibrium state. The single temperature model can't accurately reflect the changes of molecular internal energy, the gas internal energy model needs a variety of different temperatures to describe. The Three Temperature Model assumes that the translational temperature T, rotational temperature T_r and vibration temperature T_v are different [51]. Although it can accurately characterize the energy mode, the model is too complex and has a large amount of calculation, so it is not practical. Park [52] believes that in the reaction process in which air molecules participate, the translational temperature of molecules is equal to the rotational temperature, which can be described by a single temperature T, and the vibrational temperature of molecules is equal to the translational temperature of electrons, which can be described by another single temperature T_v, which is the famous Park double temperature model. This model is relatively simple and can well characterize the basic characteristics of thermodynamic nonequilibrium. It is the most widely used thermodynamic nonequilibrium temperature model at present. Considering the characteristics of high temperature flow of hypersonic vehicle, the thermodynamic double temperature model proposed by Park is used in the simulation.

3.3.2 Chemical Reaction Model

The chemical reaction models used in the numerical calculation of chemical nonequilibrium flow field include 5-component, 7-component and 11-component models. If the Mach number of the vehicle is low, the air ionization degree is relatively weak, so the plasma is thin and the electron number density is at a low level [53]. Therefore the 5-component model can accurately describe the relevant reactions. When the Mach number increases at a certain level, the 7-component chemical reaction model can be selected. When the Mach number further increases, the degree of air ionization is large, and the 11-component model can be selected. In the flight

scenario studied in this thesis, 7-component chemical reaction models are selected, and the main six chemical reaction equations are shown in Table 3.1.

Table 3.1 7-component chemical reaction equations

Number	Chemical Equation
1	$N_2 + M \rightleftharpoons N + N + M$
2	$O_2 + M \rightleftharpoons O + O + M$
3	$NO + M \rightleftharpoons N + O + M$
4	$N_2 + O \rightleftharpoons NO + N$
5	$NO + O \rightleftharpoons O_2 + N$
6	$N + O \rightleftharpoons NO^+ + e^-$

Where M is the third catalyst, or collision body, which represents the mixture formed by any one or several components in the chemical reaction model in corresponding proportion.

In the numerical calculation of hypersonic flow field using CFD-FASTRAN, in addition to the above two temperature model and 7-component chemical reaction model, the free incoming flow is set as the air composed of 79% N_2 and 21% O_2, the far-field boundary conditions are consistent with the free incoming flow, and the outlet is set as the supersonic outlet without viscous flow. There is no chemical reaction on the wall and the wall is an isothermal wall with a temperature of 1500 K, which meets the non-slip boundary condition.

3.3.3 Conservation Equations

The flow field is dominated by physical laws, which can be expressed by mass conservation equation, momentum conservation equation and energy conservation equations [54].

(1) Mass Conservation Equation

When the fluid satisfies the continuity assumption, the velocity and density are continuous and differentiable functions of space coordinates and time. The change in the total amount in any area is equal to the amount of inflow or outflow from the boundary. The conserved quantity remains unchanged, which can be expressed as

$$\frac{\partial \rho}{\partial t} + \nabla \cdot (\rho \vec{V}) = 0 \tag{3.38}$$

Where $\rho = \rho(\vec{r}, t)$ means the density of the fluid at the position vector $\vec{r}$ at time t, $\vec{V} = \vec{V}(r, t)$ means the velocity vector of the fluid at the position vector $\vec{r}$ at time t.

The mass conservation equation of each component or mixture fraction in the gas is

$$\frac{\partial \rho_s}{\partial t}+\frac{\partial}{\partial x_j}\left(\rho_s u_j\right)=-\frac{\partial J_{sj}}{\partial x_j}+\omega_s \tag{3.39}$$

Where, ρ_s is the density of the of component or mixture, J_{sj} is the mass diffusion coefficient in *j* direction, ω_s is the reaction source term related to component *s*. In inviscid flow, the mass diffusion coefficient is not considered. When there is mixing and chemical reaction in the flow field, the component conservation equation needs to be adopted, and the density of the mixture $\rho=\sum\rho_s$.

(2) Momentum Conservation Equation

The physical meaning of momentum conservation equation is that the change rate of momentum of each control body unit in the fluid to time is the same as the sum of all external forces acting on the control body unit, that is

$$\frac{\partial}{\partial t}\left(\rho u_i\right)+\frac{\partial}{\partial x_j}\left(\rho u_i u_j\right)=\frac{\partial}{\partial x_j}\left[-\left(p+\frac{2}{3}\rho k\right)\delta_{ij}+\tau_{ij}\right] \tag{3.40}$$

Where p means pressure, k means the turbulent kinetic energy, τ_{ij} is the shear stress tensor, δ_{ij} is the Kronecker delta, there $\delta_{ij}=\begin{cases}1 & i=j\\ 0 & i\neq j\end{cases}$. When describing turbulent and laminar flows, the momentum conservation equation does not include turbulent kinetic energy K. When describing inviscid flow, the right side of the equation is equal to zero.

(3) Energy Conservation Equation

Here is the energy conservation equation

$$\frac{\partial E_t}{\partial t}+\frac{\partial}{\partial x_j}\left[\left(E_t+p\right)u_j\right]=\frac{\partial q_j}{\partial x_j}+\frac{\partial q_j}{\partial x_i}\left(u_j\tau_{ij}\right)-\frac{\partial}{\partial x_j}\left(\sum_{s=1}^{ns}h_s J_{s,j}\right) \tag{3.41}$$

Where, E_t is the total energy of each control body, q_j is the heat flux along the j direction, and $\frac{\partial}{\partial x_j}\left(\sum_{s=1}^{ns}h_s J_{s,j}\right)$ represents the heat transfer caused by molecular diffusion. In the hot complete gas, the heat dissipation flux is not considered. For inviscid flow problems, the right side of the equation is zero.

3.3.4 Simulation Process by CFD-FASTRAN

In this thesis, the calculation of hypersonic thermochemical equilibrium flow is realized by CFD-FASTRAN software. The basic steps of software simulation are as follows.

(1) Mesh Design

We use the preprocessing software CFD-GEOM to construct the geometric model and mesh, and export the designed model into DTF format file.

(2) CFD-FASTRAN solution

A. Model import. Importing the model file in DTF format into FASTRAN software.

B. Module selection. Selecting compressible flow module and chemical reaction mixed fluid module.

C. Module setting. For the flow model, selecting the turbulence or laminar Navier Stokes equations model according to the actual situation. And selecting the finite rate reaction type, the double temperature non-equilibrium option for thermodynamic parameters, and the molecular database for thermodynamic attribute data. Input the 7-component air chemical reaction model.

D. Volume condition setting. For the flow field of supersonic target studied in this thesis, due to nested grid is not used, this part does not need to be changed, and the default value can be used.

E. Boundary condition setting. The incoming flow inlet is set as Inflow / outflow, and various parameters (such as speed, height, atmospheric composition, background pressure and temperature) are input according to the flight conditions of the vehicle, the object surface of the vehicle is generally selected as isothermal non slip wall, the wall temperature is usually set as 1500K, and whether to add wall catalytic conditions is selected according to the actual situation. The exit is set as the extrapolation interpolation boundary condition. If the simulation target is a rotationally symmetric body, symmetrical boundary conditions can also be set to save simulation time.

F. Set initial value condition. According to the actual situation, the inlet flow condition can generally be entered as the initial value.

G. Solution. Including the setting of solution parameters such as numerical format, integration mode, cycle times, convergence standard, simulation mode (steady-state or time-domain mode), which can be set according to the actual situation, and then start the calculation.

(3) Post processing

The post-processing software CFD-VIEW or other fluid data processing software such as Tecplot are used to output and display the simulation results of FASTRAN.

3.3.5 Simulation Results

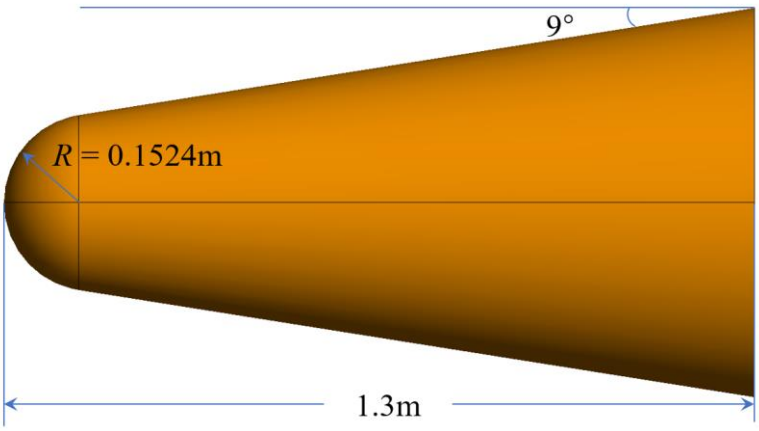

Fig. 3.5 RAMCII model

Spherical cone is a very typical simplified model of hypersonic vehicle. RAM-C series experiments in the United States have measured a lot of relevant experimental data, which makes RAM-C have a large number of numerical calculation results, and provides a lot of reference data for the calculation results of this thesis. As is shown in Fig. 3.5. The cone's head radius r = 0.1524m, half cone angle 9°, length 1.3m and attack angle is 0°. The grid used in this section is shown in Fig. 3.6, and the grids at the wall and near the shock wave detachment distance are densified. In order to compare with the experimental data, the flow field distribution of the spherical cone at 61km, 23.9Mach is numerically simulated. In each example, the flowing air is assumed to be composed of 79% N_2 and 21% O_2.

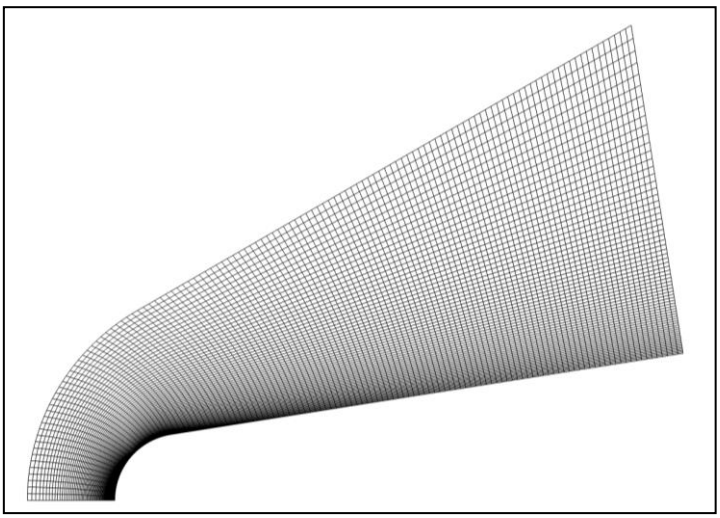

Fig. 3.6 RAM C-II flow field mesh

(1) Simulation verification

Fig. 3.7 shows the comparison of the peak electron number density along the axial direction with the experimental data when the flight Mach number is 23.9 [55]. It can be seen that the

two curves fit well, and the experimental data are scattered around the calculated peak electron number density curve, indicating the correctness of the calculated data in this thesis, and most ionization reactions occur in the stagnation point area. Therefore, the electron number density is the largest at the stagnation point of the aircraft, and then decreases along the surface of the vehicle.

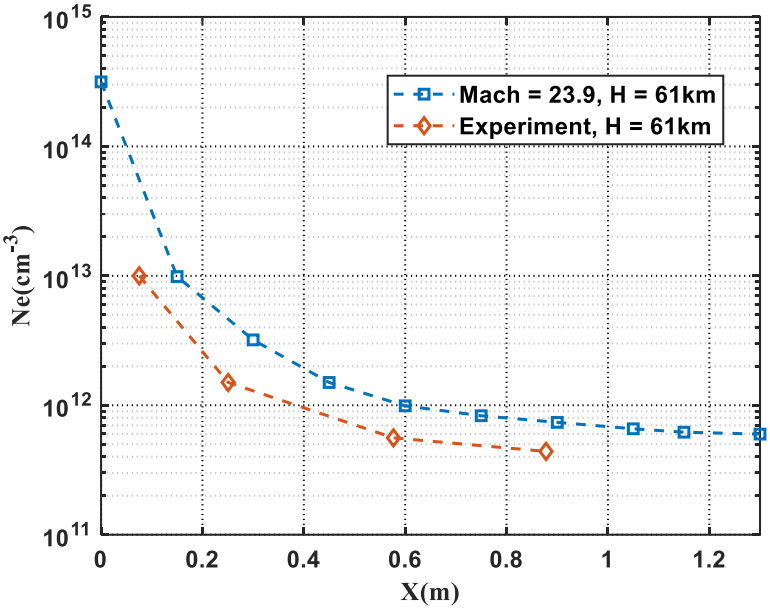

Fig. 3.7 Comparison between FASTRAN simulation data and NASA experimental data of peak electron density

(2) Simulation Result of Electric Number Density

In all the following simulation cloud diagrams, the unit of electron number density is PCS / cubic centimeter (cm^{-3}). This section simulates the chemical reaction flow of the blunt cone model at different Mach numbers and flight heights. The calculated flight heights *H* are 30, 40, 50, 60, 70 and 80 km respectively. For each height, the Mach numbers *Ma* are 9, 10, 12, 14, 16, 18, 20 and 22 Mach respectively.

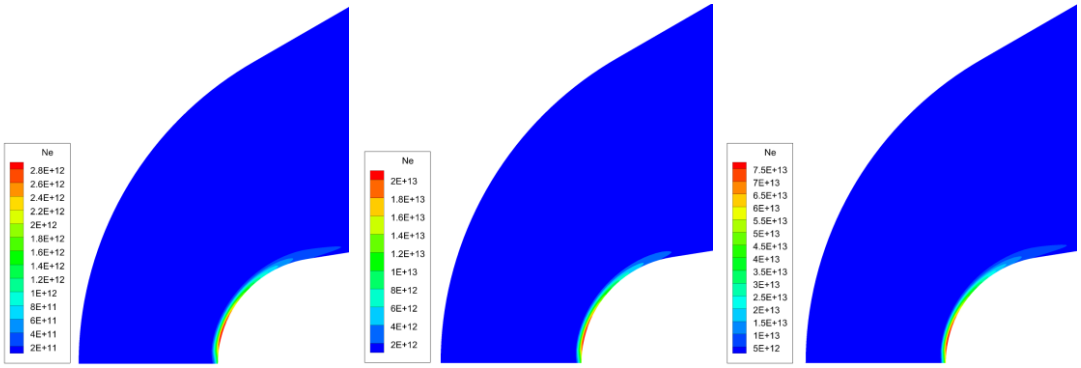

(a) *Ma* = 12 (b) *Ma* = 14 (c) *Ma* = 16

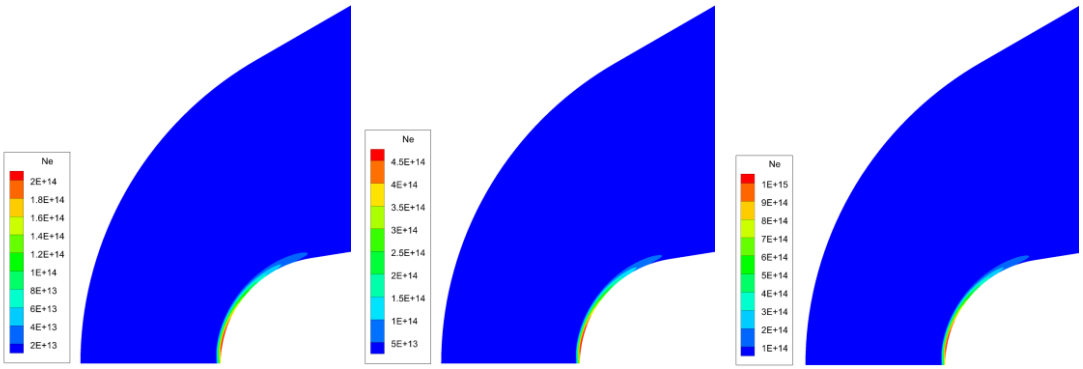

(d) *Ma* = 18 (e) *Ma* = 20 (f) *Ma* = 22

Fig. 3.8 Electron number density of blunt cone head at different flight Speeds (*H* = 50km)

Temperature is closely related to the chemical reaction in the flow field. With the increase of Mach number, the electron number density increases (See in Fig. 3.8). The electron number density is an important parameter to characterize the electrical characteristics of plasma. Its distribution determines the distribution of plasma characteristic frequency in reentry flow, which is a flow field parameter we pay special attention to. The high electron number density is at the head area, where the plasma intensity is strong. The plasma intensity in the main body area is relatively weak. Generally, the ionization degree of hypersonic reentry flow field is very low, and the ionized gas is weakly ionized plasma [56]. A large range of plasma wake area will be formed behind the tail of the reentry body, and the electron number density in this area is several orders of magnitude smaller than that of the head and body. This thesis mainly simulates the flow field around the head and body of the hypersonic reentry body with high plasma intensity, without considering the wake area with relatively weak plasma intensity. Looking at the distribution characteristics of flow field parameters shown in Fig. 3.8, the change of Mach number has little impact on the wave system structure of hypersonic blunt cone flow field, but has a great impact on the value distribution of flow field parameters. For hypersonic flow around a blunt cone, the flow field parameters generally decrease gradually from the stagnation point to the rear area.

When other reentry conditions remain unchanged, the influence of flight height change on the flow field parameters around the hypersonic blunt cone body can be reflected in Fig. 3.9. In general, the change of height mainly affects the numerical distribution of flow field parameters, but has little effect on the wave system structure of flow field. As the height increases, the pressure and density of the background atmosphere decrease, resulting in the decrease of flow field pressure and density, and the electron density also decreases.

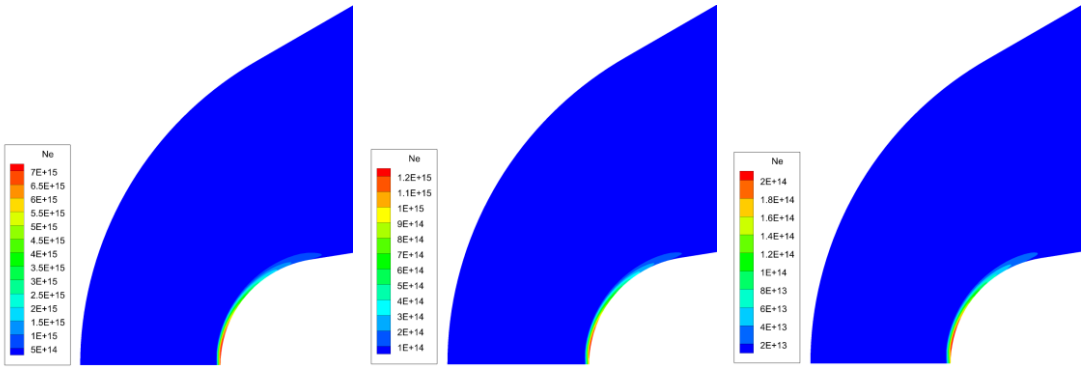

(a) H = 30km (b) H = 40km (c) H = 50km

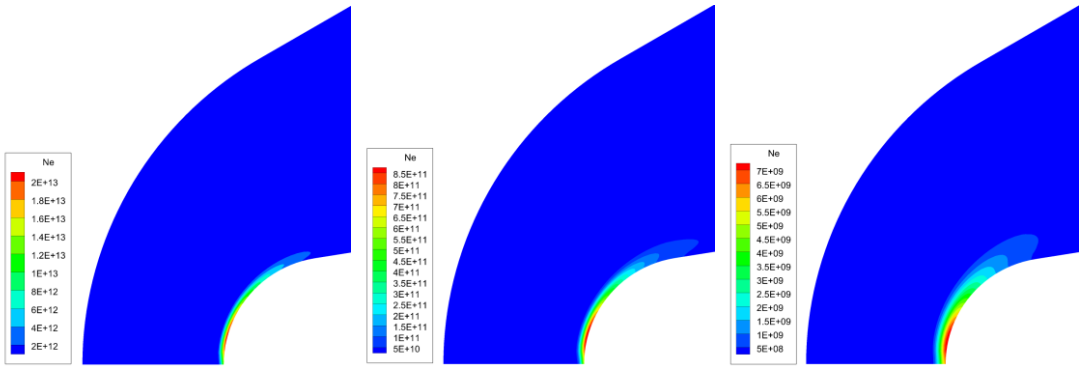

(d) H = 60km (e) *H* = 70km (f) H = 80km

Fig. 3.9 Electron number density of blunt cone head at different flight heights (*Ma* = 18)

3.4 EM Characteristics of Plasma Sheath

3.4.1 RCS Characteristics at Different Flight Heights

Fig. 3.10 shows the bistatic RCS when the EM wave with frequency of f = 3GHz is incident on the flow field around the blunt cone at 0° . The bistatic RCS curves of the flow field around the blunt cone at different flight heights and the bistatic RCS curves of the blunt cone body (labeled PEC Matlab in Fig. 3.10) and the bistatic RCS curves of the blunt cone body (PEC FEKO) calculated in FEKO are compared and given.

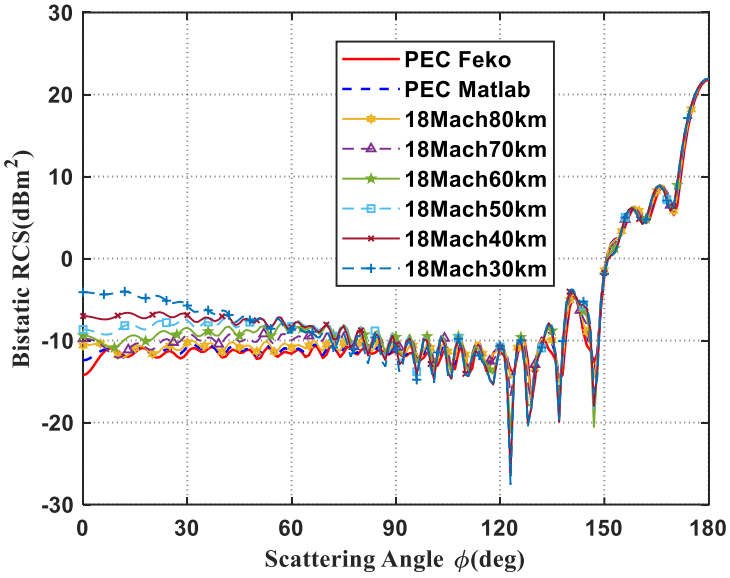

Fig. 3.10 Bistatic RCS of blunt cone flow field at different flight heights

For the same Mach number, when the height changes, the existence of the flow field around the blunt cone has a great influence on the bistatic scattering characteristics, which is mainly reflected in the variation trend of the forward and lateral bistatic RCS. When the flight altitude is no more than 80km, the presence of plasma sheath enhances the RCS in the forward direction and near both sides of the body, and the lower the flight altitude, the greater the bistatic RCS in the forward direction and near the side. When the flight altitude decreases, the atmospheric density increases. At the same flight Mach number, the plasma frequency and collision frequency in the plasma sheath increase, resulting in the enhancement of the scattering effect of the plasma on the EM wave, thus increasing the forward and lateral bistatic RCS.

3.4.2 RCS Characteristics at Different Flight Speeds

Fig. 3.11 shows the flow field around the blunt cone head and the bistatic RCS comparison curve of the blunt cone body at different Mach numbers when the height is H = 50km, the incident angle is $\theta_i = 90°$, $\varphi_i = 0°$, the scattering angle is $\theta_s = 90°$, $\varphi_s = [0°,180°]$, the incident wave frequency is $f = 3$GHz.

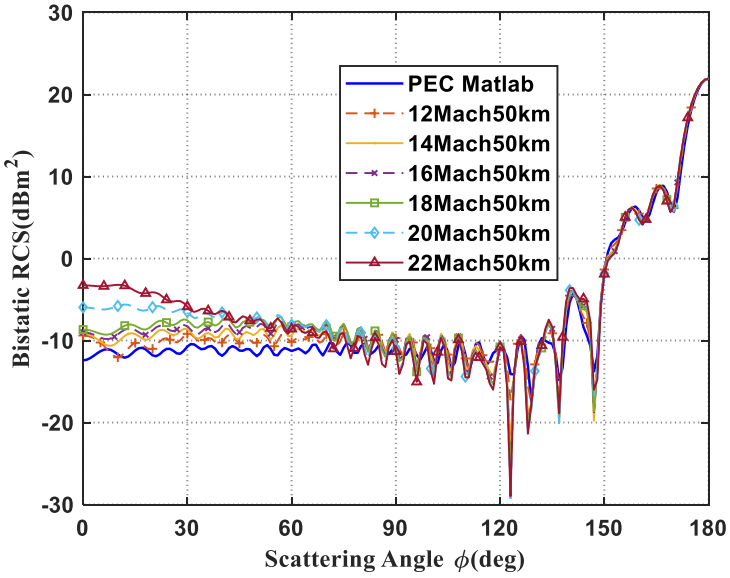

Fig. 3.11 Bistatic RCS of blunt cone flow field at different flight speeds

It can be seen from Fig. 3.11 that the change of Mach number has a great impact on the bistatic RCS scattering characteristics of the flow field, mainly affecting the RCS near the forward and lateral directions. With the increase of Mach number, the plasma intensity of the whole flow field increases, and the RCS near the forward and lateral directions increases, and the increasing range continues to increase. However, when the Mach number increases to a certain extent, the influence of the increase of Mach number on the plasma body gradually weakens, so the increase of RCS tends to weaken. When the Mach number is low, the bistatic RCS curve of the plasma sheath is generally close to the body bistatic RCS curve. This is due to the plasma intensity in the shock layer is very small when the Mach number is reduced to a certain extent, so the flow field has a great impact on the scattering characteristics of the blunt cone.

3.5 Chapter Summary

In this chapter, we study the EM scattering characteristics of the composite target of blunt cone covered by plasma sheath. Firstly, we introduce the basics of PO algorithm for coated target. Then we use FASTRAN to model and analyze the plasma sheath flow field, and obtain reliable electron number density data. Then, the electron density data is equivalent to EM data, and the PO algorithm of layered medium is applied to the plasma sheath to analyze the influence of the plasma sheath on bistatic EM scattering at different flight heights and speeds.

4 SAR Image Simulation of Tree Ground Composite Target Based on PO Algorithm

As an important natural resource, forest play a significant role for human production and daily life. Forest remote sensing has always been one of the important contents of radar remote sensing research. The main purpose of this chapter is to analyze the EM scattering characteristics of tree ground composite targets through PO algorithm, and simulate the SAR image through NUFFT method. This chapter introduces the principle of SAR imaging and the geometric and EM modeling for tree ground composite target, then analyzes scattering characteristics of a single tree. Finally present the SAR simulation image by NUFFT method.

4.1 Basics of SAR Imaging

Synthetic Aperture Radar (SAR) has become one of the most important inventions in the field of radar since World War II due to its high resolution, all-weather and all-time advantages. It uses the scattering phenomenon when the EM wave irradiates the target to detect and ranging the target. SAR has high resolution and can get a clear two-dimensional image of the detected target. High resolution here includes two meanings, high azimuth resolution and high range resolution [57].

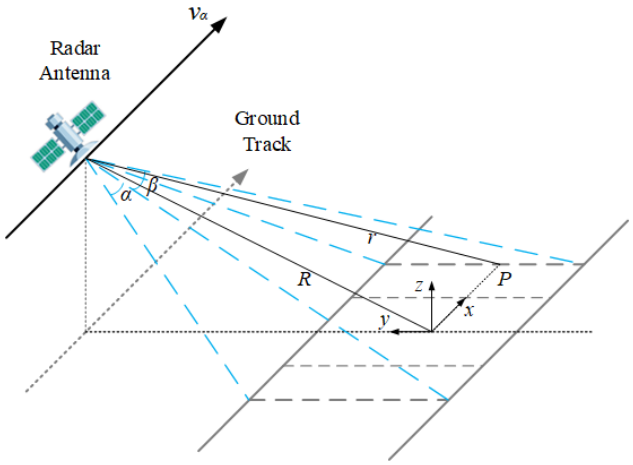

Fig. 4.1 Schematic diagram of Synthetic Aperture Radar

The antenna length L of general radar has a great influence on the azimuth division rate. Set the wavelength of the EM wave λ, then the main beam opening angle θ of the radar is λ/L. Therefore, when the distance between the target and the radar is r, the lateral resolution of the target is equal to $\lambda r/L$. SAR can effectively improve the horizontal resolution by fusing the received signals in all directions.

As shown in Fig. 4.1, the basic geometric relationship of banded SAR is given. x direction is the radar forward direction and R direction is the oblique range direction. Assuming that the forward speed of the radar is v_α, the oblique distance is R, and the x-axis coordinate of point P is X, when the radar is located at target x, and since the slant range R of general SAR is much greater than (x-X), the distance r to point target P can be expressed as:

$$r = \left[R^2 + (x-X)^2 \right]^{1/2} \approx R\left[1 + \frac{(x-X)^2}{2R^2} \right] = R\left[1 + \frac{\left(v_a t - X\right)^2}{2R^2} \right] \tag{4.1}$$

In the ideal case, the radar transmitted wave is a continuous sine wave, the signal $s_r(t)$ received by the receiver is

$$s_r(t) = \mathrm{Re}\left\{ KAe^{j\omega_c(t-\alpha)} F(x) \right\} \tag{4.2}$$

Where, K is a constant, A is the amplitude of the transmitted signal, $\omega_c(t\text{-}\alpha)$ is the phase, α is the received echo time delay,

$$\alpha = \frac{2r}{c} \tag{4.3}$$

$F(x)$ is the radar horizontal gain, ignoring the radar gain $F(x) \equiv 1$, then the equation (4.3) can be expressed as

$$s_r(t) = \mathrm{Re}\left\{ KAe^{j\omega_c(t-\alpha)} \right\} \tag{4.4}$$

In equation (4.4), the echo phase and frequency will change with time. The relationship between echo frequency and time is as follows

$$f_d(t) = \frac{-1}{2\pi}\frac{d}{dt}\left(\frac{2\omega_c r}{c} \right) = -\frac{2v_\alpha^2}{\lambda R}\left(t - t_0\right) \tag{4.5}$$

Where, $f_d(t)$ also called Doppler frequency shift, which represents the variation law of echo frequency with time. $t_0 = X/v_\alpha$ represents the time when the radar passes through point X. $\lambda = 2\pi c/\omega_c$ represents the wave length of radar wave. The Doppler shift plus carrier frequency is the instantaneous frequency of the echo.

$$f_r(t) = f_c - \frac{2v_\alpha^2}{\lambda R}\left(t - t_0\right) \tag{4.6}$$

The echo signal $s_r(t)$ can be obtained from the above equations

$$s_r(t) = \mathrm{Re}\left\{ KAe^{j\left[\omega_c t - \frac{2\pi v_\alpha^2}{\lambda R}(t-t_0)^2\right]} \right\} \tag{4.7}$$

When the carrier frequency f_c is reduced to a fixed frequency f_0, the instantaneous frequency $f_{det}(t)$ of the echo is

$$f_{det}(t) = f_0 - \frac{2v_\alpha^2}{\lambda R}(t - t_0) \tag{4.8}$$

From equation (4.8), the echo signal is a linear frequency modulation signal, and its frequency modulation slope k_α is inversely proportional to the square v_α^2 of the radar carrier speed and is directly proportional to the skew distance *R*. The angular frequency form can be expressed as

$$k_\alpha = -\frac{4\pi v_\alpha^2}{\lambda R} \tag{4.9}$$

The horizontal opening angle β of the radar beam determines the time T_s when the point target *P* is illuminated by the radar wave

$$T_s = \frac{\beta R}{v_\alpha} \tag{4.10}$$

Then the azimuth resolution ρ_α of the radar is

$$\rho_\alpha = v_\alpha T_s = \beta R \tag{4.11}$$

From above equations, the echo signal is a linear frequency modulation signal, and the azimuth resolution of the echo signal can be improved through matched filtering.

According to the properties of the matched filter, its envelope *E* is

$$E = \frac{1}{2}|KA|^2 T_s \left| \frac{\sin\left(\frac{1}{2}k_\alpha T_s t\right)}{\frac{1}{2}k_\alpha T_s t} \right| \tag{4.12}$$

Where $k_\alpha = -4\pi v_\alpha^2 / \lambda R$ is the frequency modulation slope. Normalize the envelope signal to obtain the normalized envelope signal E_n as

$$E_n = \left| \frac{\sin\left(\frac{1}{2}k_\alpha T_s t\right)}{\frac{1}{2}k_\alpha T_s t} \right| \tag{4.13}$$

Its resolution τ_α is defined as the main lobe width

$$\tau_\alpha = \frac{2\pi}{|k_\alpha| T_s} = \frac{1}{\Delta f_d} \tag{4.14}$$

The azimuth resolution ρ_α of SAR can be expressed by antenna size *D*

$$\rho_\alpha = \frac{D}{2} \tag{4.15}$$

SAR extracts the information of the target illuminated by the radar according to the return wave shape by transmitting pulse and receiving echo. The time delay α of radar received echo has the following relationship with the radial distance r from the radar to the target

$$\alpha = \frac{2r}{c} \tag{4.16}$$

When the echo delay α is greater than the radar transmission pulse width τ, the radar can distinguish targets at different distances, that is, the radar range resolution is $c\tau/2$.

The radar range resolution is related to the pulse width transmitted by the radar. However, in practical engineering practice, it is difficult for radar to transmit narrow pulses, so the range resolution is poor. SAR can effectively improve the radar range resolution by making the radar transmitted wave as linear frequency modulation signal and using matched filtering at the receiver.

By normalizing the amplitude of LFM signal, the radar transmitted signal is

$$s(t) = rect\left(\frac{t}{T}\right)\cos\left[\omega_0 t + \pi k t^2\right] \tag{4.17}$$

Where $rect(t/T)$ is the rectangular function defined between $[-T/2, T/2]$

$$rect\left(\frac{t}{T}\right) = \begin{cases} 1 & -\frac{T}{2} \le t \le \frac{T}{2} \\ 0 & else \end{cases} \tag{4.18}$$

The transmitted signal is expressed in the complex form $\varphi(t)$, then

$$\varphi(t) = u(t)e^{j\omega_0 t} \tag{4.19}$$

Where

$$u(t) = rect\left(\frac{t}{T}\right)e^{j\pi k t^2} \tag{4.20}$$

After matched filtering, the envelope of the radar received signal is

$$C_\varphi(t) \approx T\frac{\sin[\pi k t T]}{\pi k t T} \tag{4.21}$$

The main lobe width is defined as the radar range resolution ρ_r

$$\rho_r = \frac{c}{2kT} = \frac{c}{2\Delta f_s} \tag{4.22}$$

Where, Δf_s is the signal bandwidth.

4.2 EM Modeling of Tree Ground Composite Target

4.2.1 Geometric Model of Composite Target

There are several components of forest in nature, and the scatterers are irregular. It is hard to describe the tree ground composite target with fine structure [58]. In order to simplify the scatterers and ensure certain accuracy requirements, F.T. Ulaby proposed an effective forest scattering model MIMICS [59], which simplifies the forest into a three-layer structure, such as crown layer, trunk layer and ground layer [60].

(1) Geometric model of leaves

There are many shapes of leaves, such as needle, oblate, strip, etc. It's difficult to describe the structure and hard to calculate the scattering field of trees. Therefore, the regular ellipsoid model is used to simplify the geometric model of leaves, as is shown in Fig.4.2, the needle is represented by a fine ellipsoid, and the broad leaf is represented by a flat ellipsoid model [61].

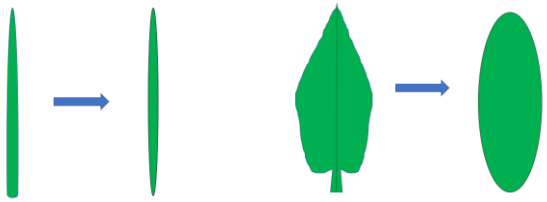

(a) Needle leaf (b) Broad leaf

Fig. 4.2 Leaf simplified model

(2) Geometric model of branch

The trees are composed of many small branches, and each branch is a long strip-shaped irregular cone. For the convenience of calculation, these twigs are described by long blunt cones, as is shown in Fig. 4.3.

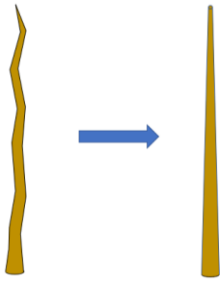

Fig. 4.3 Branch simplified model

(3) Geometric model of trunk

Compared with branches, the diameter of trunk is relatively large, which is much longer than EM wave, so it's not suitable to be expressed by long ellipsoid. The surface of the trunk is not smooth and generally rough and it will be difficult to describe these features in detail. Because

the fluctuation of the trunk surface is not very large relative to its diameter and EM wave length, its surface can be regarded as smooth. In this way, the trunk is described by a long blunt cone.

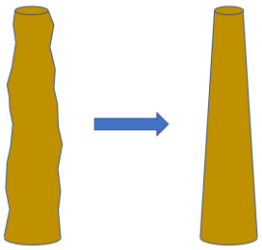

Fig. 4.4 Trunk simplified model

Finally, after the above geometric approximation, the tree ground composite model can be built in FEKO shown in Fig. 4.5. The green plate represents the land, the brown cones represent the trunk and branch, the green ellipses represent leaves. We will use this model for the calculation and imaging in the following sections.

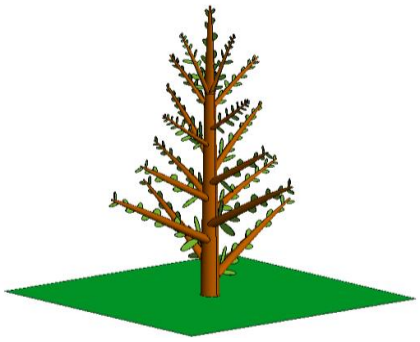

Fig. 4.5 Tree model in FEKO

4.2.2 Dielectric Constant of Composite Target

(1) Dielectric constant for tree

When studying the dielectric constant of a tree, it is usually regarded as a simple mixture of plant and water. Tree can be divided into three parts, plant body, bound water and free water [62].For the dielectric constant ε_r of plant body, in the current theoretical research, it can be obtained from the measurement results of dielectric constants from various plant materials: $1.5 \le \varepsilon_\gamma' \le 2.0,\ \varepsilon_\gamma'' \le 0.1$.

The dielectric properties of free water are basically the same as those of liquid water, and the Debye equation can be used here. The relationship between dielectric constant and frequency is as follows

$$\begin{cases} \varepsilon_f' = \varepsilon_{f\infty} + \dfrac{\varepsilon_{fs} - \varepsilon_{f\infty}}{1 + (2\pi f\tau)^2} \\ \varepsilon_f'' = \dfrac{2\pi f\tau\left(\varepsilon_{fs} - \varepsilon_{f\infty}\right)}{1 + (2\pi f\tau)^2} + \dfrac{\sigma}{2\pi\varepsilon_0 f} \end{cases} \tag{4.23}$$

Where the subscript *f* means free water, ε_{fs} is the static dielectric constant, $\varepsilon_{f\infty}$ is the dielectric constant at infinite frequency, usually taken as 4.9. $\varepsilon_0 = 8.854\times10^{-12}\,\mathrm{F\cdot m^{-1}}$ is the dielectric constant of free space. τ is the relaxation time of free water, indicating the time taken for the process of free water from the begin state of polarization to the final state. *f* is the frequency of the EM wave, σ (Siemens m^{-1}) is the conductivity of solution ions in free water. The relationship between σ and salinity *s* is $\sigma \cong 0.16s - 0.0013s^2$. Under the conditions of salinity $s \le 10$ ‰ and temperature T = 22 ℃, the equation (4.23) can be written as

$$\varepsilon_f = 4.9 + \frac{75}{1 + jf/18} - j\frac{18\sigma}{f} \tag{4.24}$$

For the dielectric constant of bound water, in order to obtain the experimental data, Ulaby et al. measured the dielectric constant of sucrose aqueous solution. The dielectric constant Debye equation of bound water is obtained from the experimental results as follows

$$\varepsilon_b = \varepsilon_{b\infty} + \frac{\varepsilon_{bs} - \varepsilon_{b\infty}}{1 + \left(jf / f_{bo}\right)^{1-\alpha}} \tag{4.25}$$

Here, subscript *b* represents bound water and α is relaxation parameter. Select Debye equation parameter suitable for measurement data, where $\varepsilon_{b\infty} = 2.9$, $\varepsilon_{bs} = 57.9$, $f_{bo} = 0.18$GHz, $\alpha = 0.5$. Then equation (4.31) can be written as

$$\varepsilon_b = 2.9 + \frac{55}{1 + (jf/0.18)^{0.5}} \tag{4.26}$$

It can be seen from the above analysis that the plant material is composed of plant body, bound water and free water, so the equation of its dielectric constant is

$$\varepsilon_v = \varepsilon_\gamma + v_{fw}\varepsilon_f + v_b\varepsilon_b \tag{4.27}$$

Where ε_v is the dielectric constant of plant, $v_{fw}\varepsilon_f$ is the volume content of free water and its dielectric constant, $v_b\varepsilon_b$ is the volume content and dielectric constant of bound water and its bound plants.

Substituting the equations (4.25) and (4.26) into the equation (4.27), the dielectric constant of plant material at room temperature T = 22℃ can be obtained

$$\varepsilon_v = \varepsilon_\gamma + v_{fw}\left[4.9 + \frac{75}{1+jf/18} - j\frac{18\sigma}{f}\right] + v_b\left[2.9 + \frac{55}{1+(jf/0.18)^{0.5}}\right] \tag{4.28}$$

Using the refraction model of two-phase mixture, the equation of vegetation dielectric constant can be written as [63]

$$\varepsilon_c^{1/2} = \varepsilon_{air} + v_v\left(\varepsilon_v^{1/2} - \varepsilon_{air}^{1/2}\right) \tag{4.29}$$

Where ε_c, ε_{air} and ε_v refer to the dielectric constants of vegetation, air and plant materials respectively, and v_v is the volume content of plant materials. Typically, the volume content of plant materials (leaves or lotus) is less than 1% of the volume of the whole vegetation.

(2) Dielectric constant for ground

Ground is a mixture of soil particles, air and water. It is also a typical target medium in the fields of microwave remote sensing and space monitoring. Understanding the dielectric properties of soil is the necessary basis for the study of scattering characteristics and parameter inversion. Therefore, it is necessary to study the dielectric properties of soil and its interaction with EM waves.

The soil model used in the calculation of vegetation environment is generally wet soil with certain moisture, so this thesis does not make a specific analysis of dry soil. The dielectric constant EPS of wet soil can be decomposed into

$$\varepsilon = k_0\varepsilon_0 + k_w\varepsilon_w + k_s\varepsilon_s \tag{4.30}$$

Where, ε_0, ε_w and ε_s represent the dielectric constants of air, water and soil particles respectively, k_0, k_w and k_s represent the proportion of these three media in the soil respectively, here $k_0 + k_w + k_s = 1$.

When establishing the ground model, the dielectric constant of the ground can be calculated from the above equation by setting the proportion of each material according to the actual situation and understanding their respective dielectric constant. In general, the dielectric constant of free water is a constant in a certain frequency range. Through actual measurement, it is usually taken as 75. The relative dielectric constant of air is 1.

4.3 NUFFT Theory

When the polarization direction of the receiving antenna is $\hat{p}$, the scalar expression of the Physical Optical far-field scattering field E_p is [64]

$$E_p = \hat{\boldsymbol{p}} \cdot \boldsymbol{E}^{(s)}(\boldsymbol{r}) = \frac{-ikZ_0 e^{ikr}}{2\pi r} \int_{S_{lit}} \hat{\boldsymbol{p}} \cdot \left[\hat{\boldsymbol{r}} \times \hat{\boldsymbol{r}} \times \left(\hat{\boldsymbol{n}}(\boldsymbol{r}') \times \hat{\boldsymbol{r}}_i \times \boldsymbol{E}^{(i)} \right) \right] dS(\boldsymbol{r}') e^{ik(\hat{\boldsymbol{r}}_i - \hat{\boldsymbol{r}}) \cdot \boldsymbol{r}'} \tag{4.31}$$

Here, due to the sum of the scattered fields of each panel constitutes the scattered field of the scatterer, we can construct the objective function as a function in the integral of equation (4.31).

$$O(\boldsymbol{r}') = \hat{\boldsymbol{p}} \cdot \left[\hat{\boldsymbol{r}} \times \hat{\boldsymbol{r}} \times \left(\hat{\boldsymbol{n}}(\boldsymbol{r}') \times \hat{\boldsymbol{r}}_i \times \boldsymbol{E}^{(i)} \right) \right] \delta\left(S(\boldsymbol{r}') \right) \tag{4.32}$$

Where $\delta(S(r'))$ is the impulse function, which is used to express whether the single patch is in the bright region.

$$S(\boldsymbol{r}') \begin{cases} = 0, \boldsymbol{r}' \in S_{lit} \\ \neq 0, \boldsymbol{r}' \notin S_{lit} \end{cases} \tag{4.33}$$

Then, E_p can be expressed as

$$E_p(\boldsymbol{k}) = \frac{-ikZ_0 e^{ikr}}{2\pi r} \iiint_{S_{lit}} O(\boldsymbol{r}') e^{-i\boldsymbol{k} \cdot \mathbf{r}'} d^3 \boldsymbol{r}' \tag{4.34}$$

Where, $\boldsymbol{k} = k(\hat{\boldsymbol{r}} - \hat{\boldsymbol{r}}_i)$. It can be seen that the scattering field $E_p(\boldsymbol{k})$ collected in the wavenumber domain ($\boldsymbol{k}$ domain) is a three-dimensional Fourier transform form of the objective function $O(\boldsymbol{r}')$, so after obtaining the scattering field $E_p(\boldsymbol{k})$ in the wavenumber domain, the estimation $O(\boldsymbol{r}')$ of the objective function $\widetilde{O}(\boldsymbol{r}')$ can be obtained by inverse Fourier transform. Substitute $\boldsymbol{k} = \hat{x}k_x + \hat{y}k_y + \hat{z}k_z$ and $\boldsymbol{r}' = \hat{x}x' + \hat{y}y' + \hat{z}z'$ into equation (4.34), we can obtain

$$\tilde{O}(x', y', z') = \frac{1}{(2\pi)^3} \iiint \frac{2\pi r}{-ikZ_0 e^{ikr}} \hat{\boldsymbol{p}} \cdot \boldsymbol{E}^{(s)}(k, \theta, \varphi) e^{i\left(k_x x' + k_y y' + k_z z'\right)} dk_x dk_y dk_z \tag{4.35}$$

The integral interval of Fourier transform is $(-\infty, +\infty)$, but in the actual scattering field sampling, it is unrealistic to carry out full interval sampling.

Therefore, the high-frequency small angle two-dimensional SAR imaging data are obtained by sampling in the wave number range [$k_{\min}$, $k_{\max}$] and azimuth angle range [$\theta_{\min}$, $\theta_{\max}$]. The two-dimensional imaging equation of discrete data is [65]

$$I(x, z) = \frac{1}{(2\pi)^2} \sum_{k_{\min}}^{k_{\max}} \sum_{\theta_{\min}}^{\theta_{\max}} \frac{2\pi r}{-ikZ_0 e^{ikr}} E^s(k, \theta) e^{ik_x x} e^{ik_z z} \tag{4.36}$$

Where, $k_x = 2k\sin\theta$, $k_y = 2k\cos\theta$. The scattered field data in the frequency domain (k, θ) is uniformly distributed, but it is non-uniformly distributed in the (k_x, k_y) domain. N-term discrete inverse Fourier transform is performed on the one-dimensional sequence with length N, and the expression is as follows

$$X_n = \frac{1}{N} \sum_{k=1}^{N} x(k) e^{j\frac{2\pi}{N} n\omega_k} \tag{4.37}$$

Where $x(k)$ is the data value to be transformed, ω_k is the normalized frequency, and N is the number of discrete points, which meets the following relationship

$$\omega_k \in \left[-\frac{N}{2}, \frac{N}{2}-1\right],\ \ k=1,2,...,N,\ \ n=-\frac{N}{2}, -\frac{N}{2}+1, ..., \frac{N}{2}-1 \tag{4.38}$$

Write $e^{j2\pi\omega_k/N}$ as the sum of successive multinomial Fourier series, that is, write each $x(k)e^{j2\pi\omega_k/N}$ as the sum of $(2Q+1)$ terms, and $x_k(\omega_k)$ as the coefficient of each term. Then there are

$$s_n e^{j\frac{2\pi}{N}n\omega_k} \approx \sum_{k=[G\omega_k]-Q}^{k=[G\omega_k]+Q} x_k(\omega_k) e^{j\frac{2\pi}{GN}nk} \tag{4.39}$$

Where Q is the oversampling factor, $s_n = \cos(\pi n/GN)$. Then one-dimensional IDFT can be rewritten as

$$\begin{aligned} X_n &= \frac{1}{N}\sum_{k=1}^{N} x(k) e^{j\frac{2\pi}{N}n\omega_k} \\ &= \frac{1}{Ns_n}\sum_{k=1}^{N} x(k)\left(\sum_{q=-Q}^{Q} x_{q+[G\omega_k]}(\omega_k) e^{j\frac{2\pi}{GN}n(q+[G\omega_k])}\right) \\ &= \frac{1}{Ns_n}\sum_{k=-\frac{GN}{2}}^{\frac{GN}{2}-1} x'(k) e^{j\frac{2\pi}{GN}nk} \end{aligned} \tag{4.40}$$

Extended to the two-dimensional case, we have

$$\begin{aligned} X_{nm} &= \frac{1}{NM}\sum_{m=1}^{M}\sum_{k=1}^{N} x(k,m) e^{j\frac{2\pi}{N}n\omega_k} e^{j\frac{2\pi}{M}n\omega_m} \\ &= \frac{1}{NMs_n}\sum_{m=1}^{M}\sum_{k=1}^{N} x(k,m)\left(\sum_{q=-Q}^{Q} x_{q+[G\omega_k]}(\omega_k) e^{j\frac{2\pi}{GN}n(q+[G\omega_k])}\right)\left(\sum_{q=-Q}^{Q} x_{q+[G\omega_k]}(\omega_m) e^{j\frac{2\pi}{GM}n(q+[G\omega_m])}\right) \\ &= \frac{1}{NMs_n}\sum_{m=-\frac{GM}{2}}^{\frac{GM}{2}-1}\sum_{k=-\frac{GN}{2}}^{\frac{GN}{2}-1} x'(k,m) e^{j\frac{2\pi}{GN}nk} e^{j\frac{2\pi}{GM}nm} \end{aligned} \tag{4.41}$$

The two-dimensional Fourier transform results can be obtained by applying the fast inverse Fourier transform to the interpolated uniform sequence $x'(k, m)$.

In order to calculate the interpolation coefficient, equation (4.41) is written in matrix form to obtain the equations of interpolation coefficient $\mathbf{x}_p(\omega_p)$, which is recorded as [66]

$$\mathbf{B}_{N\times 1} = \mathbf{A}_{N\times(2Q+1)}\mathbf{x}_{(2Q+1)\times 1} \tag{4.42}$$

The least square solution $\mathbf{x}_p^*\left(\omega_p\right)$ of the overdetermined equations is the interpolation coefficient. The interpolation coefficient of two-dimensional NUFFT is expressed as tensor matrix

$$\mathbf{x}_{km}\left(\omega_k,\omega_m\right)=\mathbf{x}_p^*\left(\omega_p\right)\otimes\mathbf{x}_q^*\left(\omega_q\right) \tag{4.43}$$

4.4 EM Scattering Analysis and SAR Imaging of Composite Target

4.4.1 EM Scattering Characteristics

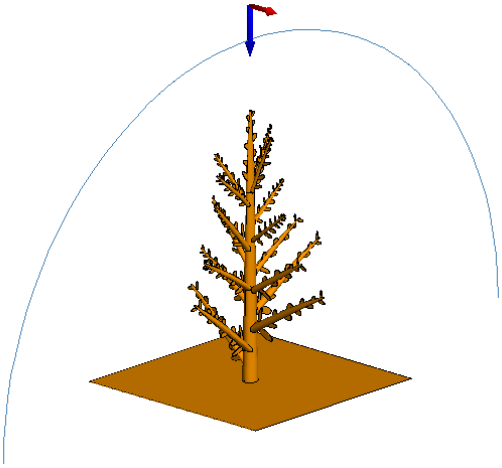

Fig. 4.6 EM scattering model in FEKO

In this section, we mainly analyze the EM scattering characteristics of tree ground composite targets. In the image shown in Fig. 4.6, we use the plane incident wave to irradiate the tree ground composite scene target from the top of the model. The incident direction of the plane wave is θ_i = 0°, φ_i = 90°. The receiving direction is θ_s = [-90°,90°], φ_s = 0°, and the incident wave frequency is 3GHz. The tree ground model is regarded as a PEC target, and the RCS EM scattering results are obtained, as shown in Fig. 4.7. We compare the data obtained by FEKO and the PO algorithm in this thesis respectively. The error of the results is in an acceptable range, we can think that the results obtained by PO algorithm is correct. The strongest value of RCS is concentrated at the scattering angle θ_s = 0°, and the scattering value tends to decrease as the angle approaches - 90°, while there are large fluctuations in the range from θ_s = 0° to 90° and from θ_s = 0° to - 90°.

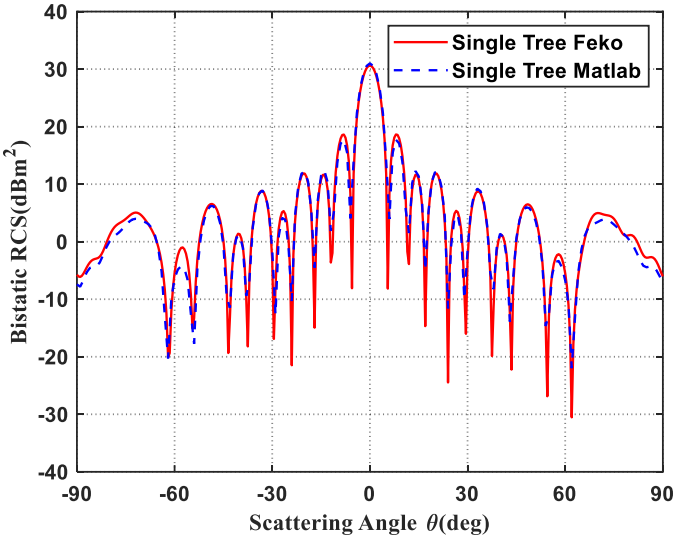

Fig. 4.7 RCS comparison of tree ground composite target (f = 3GHz, φ_s = 0)

Next, FEKO software is used to simulate and analyze the changes of RCS for tree ground composite target with different incident angles and frequencies. Based on the EM parameter modeling of tree vegetation above, we assume that the medium parameter of trunk and leaf is $\varepsilon = 1.2\text{-}j8.0\times10^{-12}$ and the medium parameter of ground soil is $\varepsilon = 75$. The geometric model of tree is shown in Fig. 4.6.

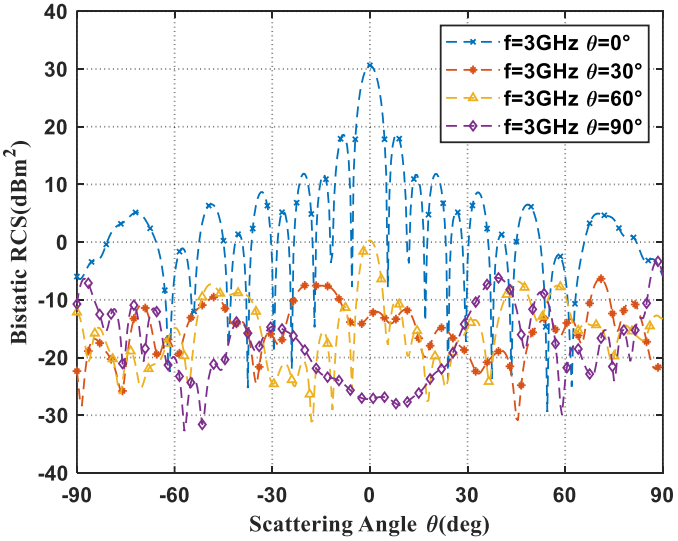

Fig. 4.8 RCS of single Tree under different pitch angle (φ_s = 0)

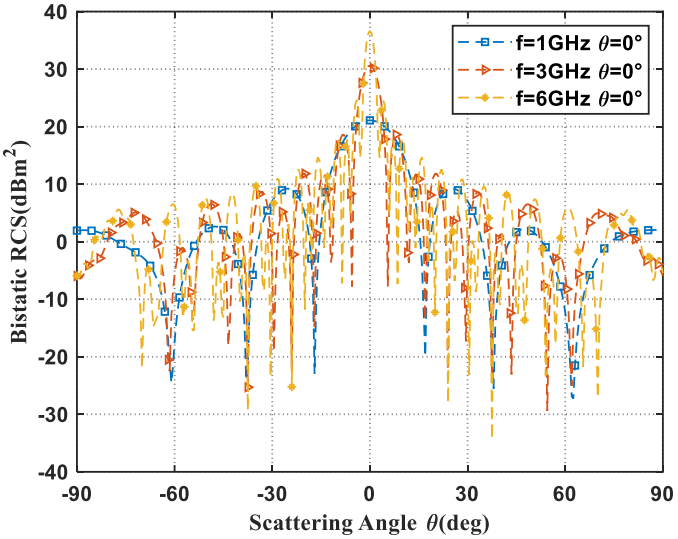

Fig. 4.9 RCS of single Tree under different frequencies ($\varphi_s = 0$)

As can be seen from Fig. 4.8, when the incident angle is 0°, the average RCS value of a single tree is the largest, especially when the scattering angle is 0°. Considering that the incident wave is irradiate on the ground and most of the incident wave energy is reflected, therefore its RCS value is the highest comparing to other scattering angles. In other incident pitch angles, the RCS value is less than 0dB, because the density of a single tree is too low and there is little refracted energy, resulting little energy received at the receiver.

In Fig. 4.9, when the frequency of the incident wave tends to increase, the RCS value will increase and the fluctuation of the RCS curve will also increase, due to the higher frequency, the greater influence of the target shape. High frequency will amplify small features of the tree ground composite target, which can be ignored at the low frequency. For example, when the low frequency incident wave irradicates the tree, we can ignore the influence of tree leaves on the scattered wave. Moreover, the average RCS value of 6GHz incident wave is higher than that of 3GHz and 1GHz.

Through the above analysis, we know that when incident from the top, most of the energy received by the receiving end is the energy reflected by the ground, so it's hard to accurately obtain the target information from the received signal. If the incident angle is 90 degrees, it means that the transmitter is on the ground to detect the tree target, which is inconsistent with the principle of SAR.

4.4.2 SAR Image of Tree Ground Composite Target

In this section, we get the SAR simulation image of tree ground composite target by NUFFT. Under the condition of a constant frequency, the facets after model segmentation will increase

along with the raise of model size. Due to the limitation of computing resources, we control the size of the target in a fix size, and reduce the tree size to increase the number of trees. The length and width of the ground are 2m, while the tree height in Fig. 4.10(a)(b)(c) are 2m, 1m and 0.5m respectively. The incident wave directions are $\theta = 60°$, $\varphi = 39°\sim51°$, 128 angles totally, and the wave frequencies are 4.7GHz~5.3GHz, 128 frequencies totally.

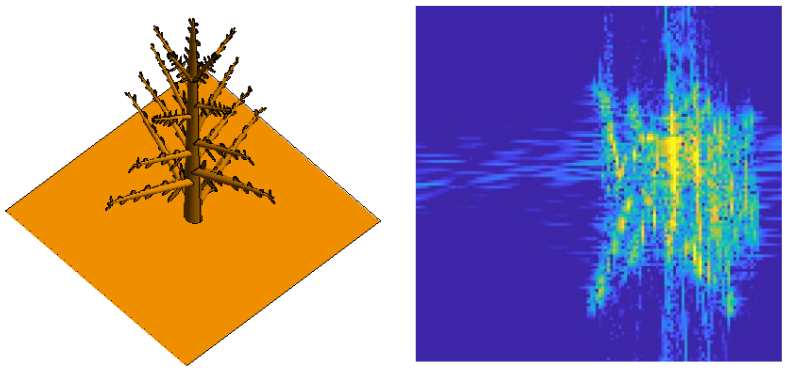

(a) FEKO model and SAR image for one tree

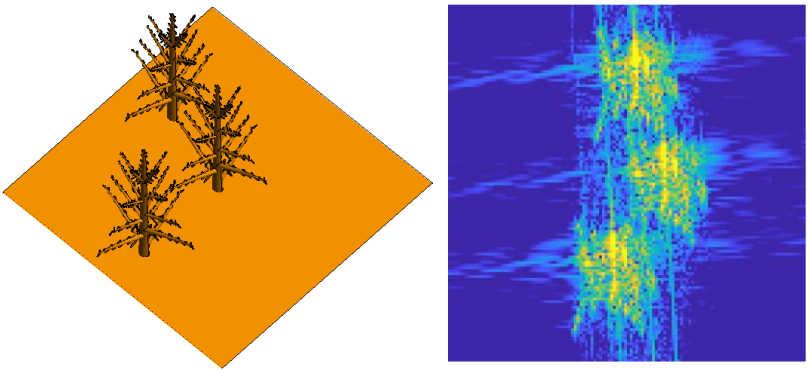

(b) FEKO model and SAR image for three trees

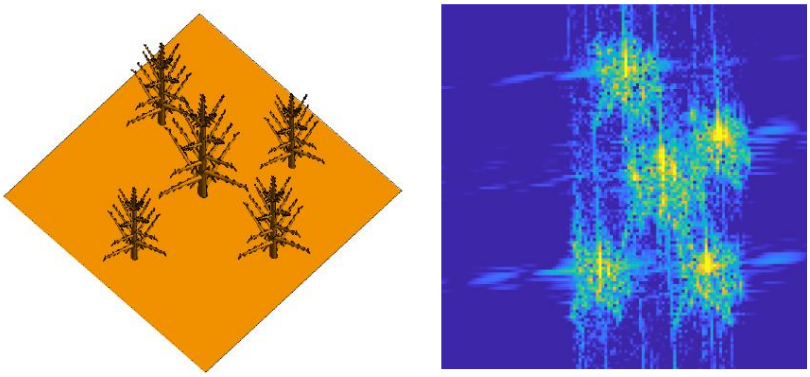

(c) FEKO model and SAR image for five trees

Fig. 4.10 SAR image simulation result of tree ground composite target

In Fig. 4.10(a)(b)(c), the left part is the model in FEKO software, and the right part is the SAR simulation image for the tree ground model. From the SAR simulated image at the right side, we can see the shape the trees, including the posture of branches and the arrangement of trees.

However, there are still a lot of clutter around the trees, and only the general outline of the trees can be seen. If the trees are too close, we may not be able to distinguish the trees. Bur in general, the simulation result is consistent with the tree model target, which laid a foundation for further research.

4.5 Chapter Summary

Firstly, in this chapter, we introduce the principle of SAR imaging, the modeling and simulation method of tree ground composite model, and the principle of NUFFT technology. Secondly, the RCS of the tree ground model is simulated and analyzed, and the RCS values of different incident angles and frequencies is obtained. Finally, the correctness of SAR imaging result can be verified by imaging the calculated data results by using NUFFT technology.

5 Conclusion

Whether in military or civil fields, composite targets are closely related to people's daily life, and the research on EM scattering characteristics of composite targets is also play an important role. In this thesis, we mainly focus on the PO occlusion judgement and EM scattering analysis of composite targets by PO algorithm. PO algorithm is widely used in the EM scattering calculation of all kinds of electrically large targets. The main idea in PO algorithm is to ignore the influence of shadow region on EM scattering and only consider the contribution of induced current in bright region. When dealing with a dielectric composite target, we regard the target as its surface coated with one or more layers of dielectric media, and use the step method to solve the reflection coefficient on the dielectric layers, so as to obtain the scattered electric and magnetic field and RCS.

5.1 Summary

In this thesis, we developed an occlusion judgement software interface for PO algorithm, which can accurately judge the edge of bright and shadow region. And we apply the PO algorithm to two kinds of composite targets, namely, plasma sheath coated hypersonic vehicle coated and tree ground composite target. The work in this thesis is summarized as follows.

1. The software interface of occlusion judgement of PO algorithm is developed. This software system is composed of interface development and visual widget development. The interface development is mainly based on Qt5 to developing buttons and text box to interact with users. The visual widget development is mainly based on OpenGL to display the 3D model and the judgement results of bright region. We use two methods to judge the bright region, they are ray tracing method and Z-Buffer method. Due to the error exists in the edge region in both two methods, we segment the edge patch to reduce the error. Finally, we compare the patch number and time consumption of the two methods after four iterations judgement, and analysis the error in Z-Buffer method.

2. Due to the PO algorithm is the core algorithm of this thesis, we use FEKO software to verify the correctness of PO method in Section 2.1.2 and Section 3.1.2 respectively. For the PEC half-sphere shell, the error of PO RCS relative to FEKO RCS is 0.3426dB, For the coating half-sphere shell, the error is 0.3963dB. Compared with the peak RCS value of 11.39dB, the error is enough to verify the correctness of PO algorithm in this thesis.

3. CFD-FASTRAN is used to simulate the flow field around the blunt cone in this thesis. From the obtained data of pressure, temperature and mass fraction, the electron number density,

plasma frequency and collision frequency of the plasma sheath can be further obtained. Then we model the plasma sheath as layered model, and finally obtain the RCS of the vehicle covered by the plasma sheath under different flight heights and speeds.

4. In the process of SAR image simulation for tree ground composite target. Firstly, we model the tree ground composite target in geometry and EM characteristics. Then we analyze the RCS under different incident angles and frequencies by PO algorithm in FEKO. Finally, the NUFFT method is used to generate the SAR image of the scattered field obtained by PO algorithm.

5.2 Prospect

In this thesis, there are still many places worthy to further study.

1. In Chapter 2, only the occlusion judgement system has been developed, so the PO algorithm can be added for EM scattering analyze in the future.

2. In Chapter 3, we only use the empirical equation to calculate the collision frequency. We can use more methods to obtain the collision frequency to study the impact of collision frequency on plasma sheath. When studying the EM scattering characteristics of plasma sheath, we only set 6 flight heights and speeds. We can add more heights and speeds to obtain more accurate analysis results.

3. In Chapter 4, the scattering results are different with various shapes of trees. In order to simulate more realistic forest SAR image, we need to consider different kinds of trees. Due to the limitation of calculation conditions, we only regard the tree ground model as PEC in the imaging process, which can be optimized in the future.

Reference

[1] R. Harrington. Field computation by moment methods [M]. Macmillan, 1968.

[2] S. Liu, L. Guo, et al. PO calculation for reduction in radar cross section of hypersonic targets using RAM [J]. Physics of Plasmas, 2018, 25(6): 062105.

[3] K. Zhou, Q. Hou, R. Wang, et al. Real-time KD-tree construction on graphics hardware [C]. ACM Transactions on Graphics (TOG), 2008: 126.

[4] J. P. Rybak, R. J. Churchill. Progress in reentry communications [J]. IEEE Transactions on Aerospace and Electronic Systems, 1971,7(5): 879-894.

[5] W. L. Grantham. Flight results of a 25000-foot-per-second reentry experiment using microwave reflectometers to measure plasma electron density and standoff distance [R]. Hampton, VA, United States: NASA Langley Research Center, 1970.

[6] W. L. Jones. Electrostatic-probe measurements of plasma parameters for two reentry flight experiments at 25000 feet per second [R]. Hampton, VA, United States: NASA Langley Research Center, 1972.

[7] R. Tang, M. Mao, K. Yuan, Y. Wang, X. Deng. A terahertz signal propagation model in hypersonic plasma sheath with different flight speed [J]. Physics of Plasmas, 2019, 26(4): 043509.

[8] X. J. Wei. SAR image simulation of typical background target [D]. Nanjing University of Aeronautics and Astronautics, 2015.

[9] X. Y. Wang. Image Simulation Research of Spaceborne Synthetic Aperture Radar Based on Imaging Mechanism [D]. Peking University, 2001.

[10] S. Niu, X. Qiu, B. Lei et al. Parameter Extraction Based on Deep Neural Network for SAR Target Simulation [J]. IEEE Transactions on Geoscience and Remote Sensing, 2020.

[11] D. Andersh. Xpatch4: the next generation in high frequency electromagnetic modeling and simulation software [C]. The Record of the IEEE 2000 International Radar Conference, 2000.

[12] J. M. Rius, M. Ferrando, L. Jofre. GRECO: Graphical electromagnetic computing for RCS prediction in real time [J]. IEEE Transactions on Antennas and Propagation, 1993, 35(4): 7-17.

[13] M. F. Catedra, J. Perez, F. S. Adana, O. Guitierrez. Efficient Ray-Tracing Techniques for 3D analysis of Propagation in Mobile Communication. Application to Picocell and Microcell Scenarios [J]. IEEE Transactions on Antennas and Propagation, 1998, 40(2): 15-28.

[14] X. Zhou, J. Y. Zhu, W. M. Yu, T. J. Cui. Time-Domain Shooting and Bouncing Rays Method Based on Beam Tracing Technique [J]. IEEE Transactions on Antennas and Propagation, 2015, 63(9): 4037-4048.

[15] G. Gal. Electromagnetic wave propagation in a lossy plasma slab with a gradient transverse to the incident wave [R]. Washington: NASA, 1970.

[16] M. P. Bachynski, B. W. Gibbs. Propagation of strong field-modulated electromagnetic waves in plasmas [R]. Washington: NASA, 1970.

[17] S. Karin, B. Denis, W. Werner. Extraction of Virtual Scattering Centers of Vehicles by Ray-Tracing Simulations [J]. 2008, 56(11): 3543-3551.

[18] V. I. Sotnikov, J. N. Leboeuf, S. Mudaliar. Scattering of Electromagnetic Waves in the Pressure of Wave Turbulence Excited by a Flow with Velocity Shear [J]. IEEE Transactions on Plasma Science, 2010, 38(2): 2208-2218.

[19] W. Michael, S. Dmitriy, F. Uwe-Carsten. Delay-Dependent Doppler Probability Density Functions for Vehicle-to-Vehicle Scatter Channels [J]. 2014, 62(4): 2238-2249.

[20] S. Safari, B. Jazi. A mathematical description for the scattering phenomena of plane wave from elliptical plasma antenna located in oblique static magnetic field [J]. The European Physical Journal Plus 132, 2017, 261.

[21] D. R. Smith, C. Y. Huang, E. Dao, S. Pokhrel and J. J. Simpson. FDTD modeling of high-frequency waves through ionospheric plasma irregularities [J]. Journal of Geophysical Research: Space Physics, 125, 2019.

[22] Y. Chang, W. F. Chen, X. J. Zeng, et al. Analysis of electromagnetic scattering characteristics of flow field around reentry blunt cone [J]. Journal of Astronautics, 2008, 29(3): 962-965.

[23] L. Nie, W. Chen, C. Xia, et al. Analysis of scattering for the flow field of a hypersonic flight vehicle [J]. Chinese Journal of Radio Science, 2014, 29(5): 874-879.

[24] C. Zhou, X. Zhang, X.C. Zhang, et al. A study of influence on warhead RCS of plasma parameters in the reentry phase [J]. Modern Radar, 2014, 36(3): 83-86.

[25] Z. Bian, J. Li, L. Guo, X. Luo. Analyzing the Electromagnetic Scattering Characteristics of a Hypersonic Vehicle Based on the Inhomogeneity Zonal Medium Model [J]. IEEE Transactions on Antennas and Propagation, 2021, 69(2): 971-982.

[26] K. F. Ji. Typical ground vehicle target SAR image simulation and evaluation [J]. Radar Science and Technology, 2010, 8(3): 223-228.

[27] X. F. Zhang, L. Q. Yang, Y. Zang. Research on Simulation Method of Ship Target SAR Image [J]. Ship electronic engineering, 2011, 31(7): 102-104.

[28] X. J. Wei. SAR image simulation of typical background target [D]. Nanjing University of Aeronautics and Astronautics, 2015.

[29] Q. C. Tao. Research on Urban Scene Modeling Based on High-resolution SAR Image and Optical Image [D]. University of Science and Technology of China, 2015.

[30] Y. T. Zhang. Building SAR image simulation method based on ray theory [J]. Foreign electronic measurement technology, 2012, 31(5): 44-48.

[31] M. M. Ren, Z. Pan, X. H. Xu. High-resolution SAR image simulation method for buildings [J]. Journal of University of Chinese Academy of Sciences, 2018, 035(6): 788-794.

[32] Z. J. Xie, H. Yue, L. M. Yuan. Fast radar image simulation method based on ray tracing [J]. Shanghai

Aerospace, 2018, 35(6): 90-94.

[33] Q. W. Li. Research on Simulation and Recognition Technology of Polarized SAR Target Image [D]. Xidian University, 2019.

[34] J. Liu, L. Guo. Fast shadowing computation for physical optics integrals in terms of levin method [J]. IEEE Antennas and Wireless Propagation Letters, 2017, 16: 1767-1770.

[35] W. Xia, Y. Wu, G. Tan, X. Ping, et al. Color Variable Speed Limit Sign Visibility for the Freeway Exit Driving Safety [C]. SAE Technical Paper 2017-01-0085, 2017.

[36] S. J. Thomas. Modulated backscatter for low-power high-bandwidth communication [D]. Duke University, 2013.

[37] N. Zhang, Y. M. Wu and Y. Yang. Recent advances on the high frequency electromagnetic modeling and simulation techniques [C]. 2017 International Applied Computational Electromagnetics Society Symposium (ACES), 2017.

[38] N. Zhang, Y. M. Wu, et al. The fast physical optics method on calculating the scattered fields from electrically large scatterers [J]. IEEE Transactions on Antennas and Propagation, 2020,68(3): 2267-2276.

[39] W. Gordon. High frequency approximations to the physical optics scattering integral [J]. IEEE Transactions on Antennas and Propagation, 2002. 42(3): 427-423.

[40] C. Qiu, G. Z. Fei, M. Y. Shi. Overview of programmable graphics hardware [J]. Journal of Communication University of China: Nature Science, 2004, 11(3):13-19

[41] B. Y. Li, M. He, X. W. Xu, et al. Fast shadowing algorithm in the MOM-PO hybrid method [J]. Journal of Microwave, 2016, 32(s1): 9-12.

[42] X. J. Dang, H. B. Yuan, N. Wang, C. H. Liang. New method for removing the hidden face in the MOM-PO hybrid method [J]. Journal of Xidian University (Natural Science), 2012, 39(1): 38-41.

[43] J. T. Li, L. X. Guo. Research on electromagnetic scattering characteristics of reentry vehicles and blackout forecast model [J]. Journal of Electromagnetic Waves and Applications, 2012, 26(13): 1767-1778.

[44] H. Li. Research on modeling method of electromagnetic scattering based on hardware and software Z-Buffer [D]. Southeast University, 2017.

[45] A. Wu, Y. M. Wu, Y. Yang, et al. The MoM-PO hybrid method for calculating the scattered field of multi-scale composite targets [J]. Chinese journal of radio science, 2019, 34(1): 83-90.

[46] J. T. Li, L. Guo. Research on electromagnetic scattering characteristics of reentry vehicles and blackout forecast model [J]. Journal of Electromagnetic Waves and Applications, 2012, 26(13): 1767-1778.

[47] E. P. Bartlett, R. M. Kendall. An analysis of the coupled chemically reacting boundary layer and charring ablator. Part III: non-similar solution of the multicomponent laminar boundary layer by an integral matrix method [M]. Washington: NASA, 1968.

[48] F. Mustafa, A. M. Hashim. Properties of electromagnetic fields and effective permittivity excited by

drifting plasma waves in semiconductor-insulator interface structure and equivalent transmission line technique for multi-layered structure [J]. Progress In Electromagnetics Research, 2010, 104: 403-425.

[49] P. M. Bellan. Fundamentals of Plasma Physics [M]. Oxford: Cambridge University Press, 2004.

[50] C. C. Hua. Numerically simulation of non-equilibrium of hypersonic vehicle and analyze the distribution of plasma in flow field [D]. Xidian University, 2013.

[51] Z. Hou, Z. Tao, Y. Xiong. Multiphysics modeling and simulation of plasma sheath [C]. URSI Asia-Pacific Radio Science Conference (URSI AP-RASC), 2016.

[52] C. Park. Assessment of two-temperature kinetic model for ionizing air [J]. Journal of Thermophysics and Heat Transfer, 1989, 3(3): 233-244.

[53] J. M. Zhang, C. R. Lu, Y. G. Guan, W. D. Liu. Thermodynamic properties and transport coefficients of air thermal plasmas mixed with ablated vapors of Cu and polytetrafluoroethylene [J]. Physics of Plasmas, 2015, 22(10): 103518.

[54] Q. Wang, et al. Design optimization of molds for autoclave process of composite manufacturing [J]. Journal of Reinforced Plastics and Composites, 2017, 0(0): 1-13.

[55] Y. S. Zhang and J. E. Scharer. Plasma generation in an organic molecular gas by an ultraviolet laser pulse [J]. Journal of Applied Physics, 1993, 73(10): 4779.

[56] H. Sun, Z. Cui, et al. Analysis of electromagnetic scattering characteristics of plasma sheath surrounding a hypersonic aerocraft based on high-order auxiliary differential equation finite-difference time-domain [J]. Physics of Plasmas, 2018, 25(6): 063514.

[57] L. Du, H. W. Liu, Z. Bao. Radar HRRP Statistical Recognition: Parametric Model and Model Selection [J]. IEEE Transactions on Signal Processing, 2008, 56(5): 1931-1944.

[58] C. J. Willis. Target modelling for SAR image simulation [C]. SPIE Remote Sensing, 2014.

[59] F. T. Ulaby, et al. Michigan microwave canopy scattering model [J]. International Journal of Remote Sensing, 1990, 11(7): 1223-1253.

[60] A. Tour, et al. Adaptation the MIMICS backscattering model to the agricultural contex-wheat and canola at L and C bands [J]. IEEE Transactions on Geoscience and Remote Sensing, 1994, 32(1): 47-61.

[61] X. Husson, T. Lepetit, et al. Dynamic 3D Model of a Tree for High-Resolution SAR Imaging [C]. 13th European Conference on Synthetic Aperture Radar (EUSAR 2021), 2021.

[62] R. Prajapati, S. Kumar, and S. Agrawal. Simulation of SAR backscatter for forest vegetation [C]. SPIE Asia-Pacific Remote Sensing, 2016.

[63] F. T. Ulaby, R. K. Moore, A. K. Fung. Microwave Remote Sensing: Active and Passive, Vol. III -- Volume Scattering and Emission Theory [M]. Massachusetts, 1986.

[64] Y. Zhu, et al. Nufft-Based Algorithm for Bistatic Sar Imaging Via Cooperative High-Orbit and Low-Orbit Satellites [C]. IEEE International Geoscience and Remote Sensing Symposium (IGARSS 2019), 2019.

[65] J. I. Lee, D. W. Seo. Improvement of Computational Efficiency for Fast ISAR Image Simulation Through Nonuniform Fast Fourier Transform [J]. IEEE Antennas and Wireless Propagation Letters, 2021: 1-1.

[66] X. Meng, S. Wu, T. Li, H. Zhang. Circular SAR cylindrical area reconstruction using omega-k algorithm based on NUFFT [C]. IEEE 9th UK-Europe-China Workshop on Millimeter Waves and Terahertz Technologies (UCMMT), 2016.

Publications in Master Study

[1] C. M. Wang and Y. M. Wu. Research on Electromagnetic Modeling of Plasma Sheath by the Efficient Fast Physical Optics Method [C]. 2021 International Conference on Microwave and Millimeter Wave Technology (ICMMT), 2021, pp. 1-3.